Eberhard Karls Universität Tübingen
Mathematisch-Naturwissenschaftliche Fakultät
Fachbereich Geowissenschaften

Bachelor thesis

Experimental analysis of the Monin-Obukhov similarity theory in the lower surface layer

Maren Haid

August 10, 2013

1st examiner: Prof. Dr. Jens Bange
2nd examiner: Dr. Daniel Martinez Villagrasa (supervisor)

Eigenständigkeitserklärung

Hiermit bestätige ich, dass diese Bachelorarbeit vollständig von mir und in meinen eigenen Worten verfasst wurde. Ich versichere, dass keine anderen Quellen und Hilfsmittel benutzt wurden und dass ich Stellen, die dem Wortlaut oder dem Sinn nach anderen Werken entnommen sind, eindeutig gekennzeichnet habe. Ferner war diese Arbeit weder vollständig noch in wesentlichen Teilen Gegenstand eines anderen Prüfungsverfahrens.

Ort, Datum:

Unterschrift:

Contents

List of Figures

List of Tables

For eight levels within the lowest 2 m above ground level, dimensionless gradients were calculated. The time periods for which the data is used were carefully chosen, whereupon steady state conditions, horizontal homogeneity and fair weather conditions were set as requirements. For unstable conditions, it was not possible to state steady state conditions. Therefore only stable conditions were considered. An universal function was fitted through the dimensionless gradients of the upper four measurement heights for which Monin-Obukhov similarity theory is applied. Deviations to the universal function from KANSAS experiment were found. The turbulent fluxes were detected as the measurement variables with the highest probability to be responsible for these deviations. Therefore constant ‘correction factors’ of 2.16 for the turbulent heat flux and 2.15 for the friction velocity were calculated. These factors are unusable for the lowest measurement heights. It could be shown that for these heights no similarity is given. A possible physical explanation arises from the assessment of the temperature gradients, which are too small in order to balance the decreasing measurement height.

1. Introduction

To describe the spreading of micro pollutants or to do weather forecasts, atmospheric models are essential. The effort of these models is to describe the behaviour of atmospheric parameters as exactly as possible. Therefore physical laws are necessary. But since the knowledge of the governing physics of the atmosphere is insufficient to derive laws based on first principles (Stull, 1988) other ways have to be found. One method consists of similarity theories, which are based on the fact that boundary layer observations frequently show consistent and repeatable characteristics. They can then be used to derive empirical relationships for the variables of interest. One example for such a theory is the Monin-Obukhov (M-O) similarity theory. It is derived by dimensional analysis and describes the flux-profile relationship of momentum, heat, moisture and micro pollutants in non neutral stratification. In the past years, this theory was already intensively studied for measurement heights much higher than the aerodynamic roughness length (Foken, 2006). The reason for this is that there is a vertical limitation of the M-O similarity theory for these heights. As only two papers are published which analyse the M-O similarity theory for heights close to the aerodynamic roughness length, there is no real knowledge of the behaviour of this theory for lower measurement levels. Therefore the original aim of this bachelor thesis was to do an experimental analysis of the M-O similarity theory for temperature measurements within the first 2 m above ground level (AGL). Since there were measurement heights in eight different levels in this 2 m over grass, it is possible to assess M-O similarity theory for heights much higher than the roughness length and close to it.
In a first section an overview of the mathematical and physical background is given. After that the instrumentation and the measurement site are described, with special re-

gard to the thermocouples used in the field experiment. In addition, the mesoscale wind circulation for the area is described since it is used to filter the data for fair weather conditions. In the next section, the implementation to the data is reproduced, whereupon great importance is attached to the selection of the time periods. Since the universal function for the M-O similarity theory for measurement heights much higher than the aerodynamic roughness length is not consistent with the theoretical one, the focus had to be deflected to the correction of the measured variables.

2. Mathematical and physical background

2.1. Atmospheric boundary layer

The atmospheric boundary layer (ABL) is the layer which is settled above the earth's surface with a varying depth from hundreds of meters to a few kilometres. It is defined *as that part of the troposphere that is directly influenced by the presence of the earth's surface and responds to surface forcing with a time-scale of about one hour or less* (Stull, 1988). The air masses within this layer can be assumed as permanently turbulent and therefore be described with the physics of turbulent flow (Etling, 2008). Garratt (1994) compared the structure of the ABL with the two-dimensional turbulent boundary layer generated in a wind tunnel. Mainly two regions have to be distinguished: the outer (Ekman) region and the inner (surface) layer; whereas the inner layer is divided into the inertial sublayer (Prandtl layer, see section 2.4) and the interfacial (roughness) layer. Figure 2.1 gives an overview of these layers and their corresponding depths. The inner layer is highly dependent on the surface characteristics and is not much affected by the earth's rotation. The outer region shows only little sensitivity towards the roughness characteristics of the surface and Coriolis force is of importance there. The measurements this bachelor thesis deals with were gathered up to a height of 9 m. This means all data were sampled within the inner layer. The roughness layer describes the air masses just above the roughness elements comprising the land surface. In these few millimetres just above the surface, molecular diffusion is the main process for heat and mass exchange between the air and the surface (Garratt, 1994).

2.2. Basic governing equations

There are five basic equations which form the basis for boundary layer meteorology: i) equation of state, ii) conservation of mass, iii) conservation of momentum, iv) conservation of moisture and v) conservation of heat. Additionally to them equations for conservation of scalar quantities such as pollutant concentration may be added (Stull, 1988). As a starting point for turbulent derivations, most often the equation for conservation of momentum , also known as the Navier-Stokes equation, is used in its following

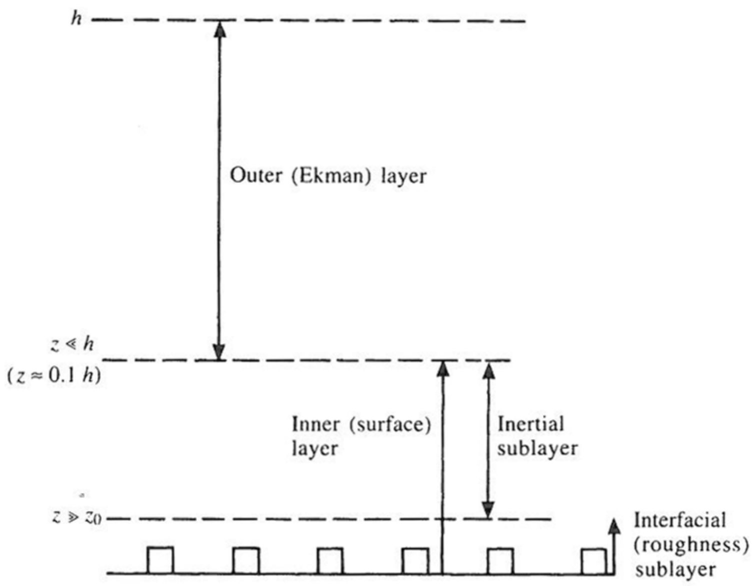

Figure 2.1: *Structure of the ABL for aerodynamically rough flow in neutrally stratified conditions. The two main layers (outer (Ekman) layer and inner (surface) layer) are labelled and corresponding depths are given. h is the depth of the ABL, z the height and z_0 is the aerodynamic roughness length. The Ekman layer is the outer region in which the surface characteristics no longer have much influence role. The surface layer consists of an inertial sublayer and an interfacial (roughness) sublayer. The flow within these two lowest layers strongly depends on the surface structure (from Garratt, 1994).*

form (Stull, 1988):

$$\frac{\partial U_i}{\partial t} + U_j \frac{\partial U_i}{\partial x_j} = -\delta_{i3} g + f_c \varepsilon_{ij3} U_j - \frac{1}{\rho} \frac{\partial p}{\partial x_i} + \nu \frac{\partial^2 U_i}{\partial x_j^2}. \tag{2.1}$$

The equation is given in Einstein's summation notation. It is an equation of motion and gives the acceleration of the air in terms of the sum of several forces (Garratt, 1994). The two terms on the left hand site (l.h.s.) represent the storage and the advection of momentum, respectively. Terms for the vertically acting gravity, the influence of the earth's rotation, the pressure-gradient forces and the influence of viscous stress follow on the right hand site (r.h.s.) (Stull, 1988). As an equation of motion, the Navier-Stokes equation contains time and space derivatives. These derivatives require initial and boundary conditions for an analytical solution. However, there are not sufficient initial and boundary conditions to resolve all turbulent scales down to the smallest eddies. For this reason the common procedure is to pick some cut-off eddy sizes below which only the statistical effects of turbulence are included.
In order to get the equation for mean momentum in a turbulent flow, equation (2.1) is statistically averaged over the smaller eddy sizes. This procedure contains several steps which will be shortly commented and which are following the description from

Stull (1988). In a first step, the Boussinesq approximation is done for the Navier-Stokes equation. The Boussinesq approximation neglects density fluctuation in the pressure-gradient force term ($\rho \approx \overline{\rho}$), but keeps them in the gravity term ($g \approx g + \rho'/\overline{\rho}g$). From the equation of state the relationship $\rho'/\overline{\rho} = -\theta_v'/\overline{\theta_v}$ can be derived. Therefore the gravitational acceleration in equation (2.1) is usually expressed by $g \approx g - \theta_v'/\overline{\theta_v}g$ (Foken, 2006). In this term the temperature is expressed by the virtual potential temperature. The potential temperature θ is used to correct the temperature for its change caused by the pressure decrease with height. It is defined as the temperature a parcel of air would have if it is brought adiabatically from its initial pressure p to a reference pressure p_0, typically 1000 hPa. Since moist air is less dense than dry air, the buoyancy caused by moisture is important. To account for this effect, the virtual temperature T_v is used (Foken, 2006). It is the temperature of dry air having the same pressure and density as moist air at temperature T (Wyngaard, 2010):

$$T_v = T(1 + 0.61 \cdot q), \tag{2.2}$$

where q is the specific humidity which is defined as the mass ratio of water vapour contained in a volume of air compared to its total mass. With equation (2.2) θ_v is defined as:

$$\theta_v = \theta(1 + 0.61 \cdot q). \tag{2.3}$$

The next step in order to reach the equation for mean momentum in a turbulent flow is the application of the Reynolds' decomposition. This is a statistical method which allows the expansion of variables into their mean and turbulent part ($U = \overline{u} + u'$). Then the whole equation is averaged and the Reynolds averaging rules are applied. At least, the turbulent advection term has to be brought into its flux form and finally the equation for the mean motion within a turbulent flow results in the following form:

$$\frac{\partial \overline{u}_i}{\partial t} + \overline{u}_j \frac{\partial \overline{u}_i}{\partial x_j} = -\delta_{i,3} g + f_c \epsilon_{ij3} \overline{u}_j - \frac{1}{\overline{\rho}} \frac{\partial \overline{p}}{\partial x_i} + \nu \frac{\partial^2 \overline{u}_i}{\partial x_j^2} - \frac{\partial \overline{u_i' u_j'}}{\partial x_j}. \tag{2.4}$$

The comparison of this equation and equation (2.1) shows that they look very similar except for the last term on the r.h.s.. This term represents the Reynolds stress on the mean motion and can be described as the divergence of the turbulent momentum flux. It is a new unknown term of second order. If an equation is constructed for this second-order moment, further terms in the form of third-order moments will arise. It can be generally expressed that an equation for the nth order moment contains terms of the $(n+1)$th order. This means it is fundamentally impossible to close the set. This problem is known as the *closure problem* and it implies that the higher-order moment terms must be parametrized in terms of known quantities (Garratt, 1994). One parametrisation is the K-theory which will be explained and used in section 2.5.

2.3. Turbulent kinetic energy

The turbulent kinetic energy (TKE) is one of the most important variables in micrometeorology because it is a measure of the intensity of turbulence and it is directly related to the transport of momentum, heat and moisture through the ABL (Stull, 1988). The mean kinetic energy per unit mass $\overline{u_i^2}/2$ of a turbulent flow can be divided in its mean part $\overline{u}_i^2/2$ and its turbulent part $\overline{u_i'^2}/2$ known as the turbulent kinetic energy $\overline{e}$ (Etling, 2008):

$$\frac{\overline{u_i^2}}{2} = \frac{\overline{u}_i^2}{2} + \frac{\overline{u_i'^2}}{2} \tag{2.5}$$

$$\overline{e} = \frac{\overline{u_i'^2}}{2} = \frac{1}{2}(\overline{u'^2} + \overline{v'^2} + \overline{w'^2}), \tag{2.6}$$

where u, v and w are the spatial components of the vector of momentum. The method which is described here in order to reach the prognostic equation for turbulent kinetic energy is taken from Etling (2008). Expression (2.5) shows that the equation of turbulent kinetic energy can be derived by subtracting the kinetic energy of the mean flow $\overline{u}_i^2/2$ from the mean kinetic energy of a turbulent flow $\overline{u_i^2/2}$, as can be seen above. The first term, $\overline{u}_i^2/2$, is derived by taking the Boussinesq approximation for equation (2.1), multiply it with u_i and taking the average. To get $\overline{u_i^2/2}$, equation (2.4) is also multiplied with u_i and again the average is taken. Finally the prognostic equation for turbulent kinetic energy is reached:

$$\frac{\partial \bar{e}}{\partial t} + \underbrace{\frac{\partial}{\partial x_j}\left\{\bar{u}_j\bar{e} + \overline{u_j' e} - \nu\frac{\partial \bar{e}}{\partial x_j} + \frac{1}{\tilde{\rho}}\overline{u_j' p'}\right\}}_{\text{Divergence of energy fluxes}} = \underbrace{-\overline{u_j' u_i'}\frac{\partial \bar{u}_j}{\partial x_j} + \frac{g}{\overline{\theta}_v}\overline{u_i'\theta_v'} - \nu\overline{\frac{\partial u_i'}{\partial x_j}}}_{\text{Production and dissipitation of turbulent energy}} \quad , \tag{2.7}$$

where the first term on l.h.s is the local change in time of the TKE. The terms which are embraced as divergence of the energy fluxes are the advection of TKE, its transport, the molecular diffusion of TKE and the pressure correlation term (Etling, 2008). These terms neither contribute to the production nor to the dissipation of turbulent kinetic energy, they are rather redistribution terms. On the contrary, the terms on the r.h.s. are production and dissipation terms of the TKE equation. The first one describes the mechanical production of TKE due to wind shear. The second one is called buoyancy term and describes the consumption and production of TKE due to buoyancy. The last term on the r.h.s is called viscous dissipation term and describes the consumption of TKE by molecular friction. It is typically labelled with ϵ:

$$\epsilon = \nu\overline{\frac{\partial u_i'}{\partial x_k}}. \tag{2.8}$$

This term is always a loss term and describes the conversion of turbulent kinetic energy to heat by molecular friction. It is the greatest for the smallest size eddies (Stull, 1988).

In order to estimate the vertical behaviour of the TKE, $i = 3$ is set in further considerations. The buoyancy term includes the vertical kinematic turbulent heat flux $\overline{w'\theta_v'}$, the gravitational acceleration g and the potential virtual temperature θ_v. The kinematic turbulent heat flux is the heat flux H divided by a constant air density ρ_{air} and the specific heat capacity of air at constant pressure c_p.
With a first estimation of the dimensions of the different terms, the terms for the divergence of energy fluxes on the l.h.s. of equation (2.6) can be neglected compared to the production and dissipation terms on the r.h.s. (Foken, 2006). Therefore the main terms influencing the turbulent kinetic energy evolution are the energy dissipation by molecular friction, the shear of the mean flow and the buoyancy forces. With the assumption of horizontal homogeneity ($\partial/\partial x = \partial/\partial y = 0$), neglecting subsidence ($\overline{w} = 0$) and a mean flow only in x-direction, equation (2.7) can be simplified to the following shape:

$$\frac{\partial \overline{e}}{\partial t} = \frac{g}{\overline{\theta}_v}(\overline{w'\theta_v'}) - (\overline{w'u'})\frac{\partial \overline{u}}{\partial z} - \epsilon. \tag{2.9}$$

In order to study the behaviour of TKE depending on the buoyancy force and wind shear, the energy dissipation ϵ is neglected (Foken, 2006):

$$\frac{\partial \overline{e}}{\partial t} = \frac{g}{\overline{\theta}_v}(\overline{w'\theta_v'}) - (\overline{w'u'})\frac{\partial \overline{u}}{\partial z}. \tag{2.10}$$

The ratio of the buoyancy term and the shear production therm is called Flux Richardson number Rf:

$$\mathrm{Rf} = -\frac{\frac{g}{\overline{\theta}_v}\overline{w'\theta_v'}}{-(\overline{w'u'})\frac{\partial \overline{u}}{\partial z}}. \tag{2.11}$$

Rf is a dimensionless parameter which can be used as a stability parameter. The shear production of energy in the denominator is always positive and symbolises the mechanical term. So Rf is positive for a negative buoyancy term and negative for a positive one. As a result, $\mathrm{Rf} < 0$ is valid for unstable stratification and $\mathrm{Rf} > 0$ for stable conditions, since a positive buoyancy term leads to production of turbulence whereas a negative term dumps the turbulence. This relationship between the production and dissipation of turbulence, respectively can be seen by means of the signs of these terms in equation (2.10). But there is a special situation for $0 < \mathrm{Rf} < 1$. Equation (2.10) shows that in this case the shear production term is bigger than the attenuation due to a negative buoyancy term and there is a positive rate of TKE. That means that the turbulence kinetic energy increases although the flow has a thermally stable stratification. The Richardson flux number of one is called the critical Richardson flux number and represents the critical value between production and consumption of turbulence.

2.4. The Prandtl layer

The Prandtl layer was already introduced in section 2.1 as the intertial sublayer and therefore as the part of the ABL which depends strongly on the characteristics of the earth's surface and where Coriolis forces can be neglected. The neglect of the influence of the earth's rotation is acceptable until a height of 50 m (Etling, 2008), since the other terms of the Navier-Stokes equation (2.1) overbalance the Coriolis force. For the consideration of the Prandtl layer it is further assumed that the force of viscous stress and horizontal pressure gradient are balanced and can therefore be neglected. Furthermore, steady state conditions ($\partial \overline{u}_i / \partial t = 0$) and horizontal homogeneity ($\partial/\partial x = \partial/\partial y = 0$) are assumed. With the implementation of all these assumptions on the horizontal component ($i = 3$) of equation (2.4) and a flow in x-direction, the following equation is reached:

$$\frac{\partial \overline{w'u'}}{\partial z} = 0. \tag{2.12}$$

This means that within the Prandtl layer, the turbulent flux of momentum $\overline{w'u'}$ and therefore the turbulent shear stress $\tau = -\overline{\rho}\overline{w'u'}$ can be assumed as constant with height over a flat, homogeneous land surface. Considering the amount of assumptions which have been made to reach this statement, it is only true for a layer of approximately 20 to 50 m above the earth's surface (Etling, 2008). Therefore, an alternative definition for the Prandtl layer is that the absolute value of the shear stress does not change more than 10 % of its surface value $(\overline{w'u'})_0$. The turbulent momentum flux at the surface is usually expressed with the friction velocity u_*:

$$u_* = \sqrt{-(\overline{w'u'})_0} = \sqrt{\frac{\tau_0}{\overline{\rho}}}. \tag{2.13}$$

Beside the Richardson number (2.11), another stability parameter exists within this layer which can be derived from the TKE equation, the Obukhov length L. It is usually used as a scaling parameter. In order to reach this parameter, the buoyancy term of the TKE equation (2.7) is multiplied by $-\kappa z/u_*^3$. Additionally, the surface values for the turbulent fluxes are used because they are considered constant within the surface layer. κ is the von Kármán constant. This leads to a dimensionless height which will further labelled as ς (Stull, 1988):

$$\varsigma = \frac{z}{L} = \frac{-\kappa z g (\overline{w'\theta_v'})_0}{\overline{\theta_v} u_*^3}. \tag{2.14}$$

where the Obukhov length is given by:

$$L = -\frac{\overline{\theta_v} u_*^3}{\kappa g (\overline{w'\theta_v'})_0}. \tag{2.15}$$

The Obukhov length can be interpreted as the height of an air column where the production ($L > 0$) or dissipation ($L < 0$) of turbulent kinetic energy caused by buoyancy is the same as the mechanical production of TKE per unit mass (Bernhardt, 1995). For stable stratification, L is positive due to a positive heat flux ($(\overline{w'\theta_v'})_0 > 0$), whereas the Obukhov length gets negative for unstable stratification ($(\overline{w'\theta_v'})_0 < 0$). For the neutral case, L goes to infinite (Etling, 2008).
Figure 2.2 shows the evolution of the Obukhov length over a diurnal cycle with stable

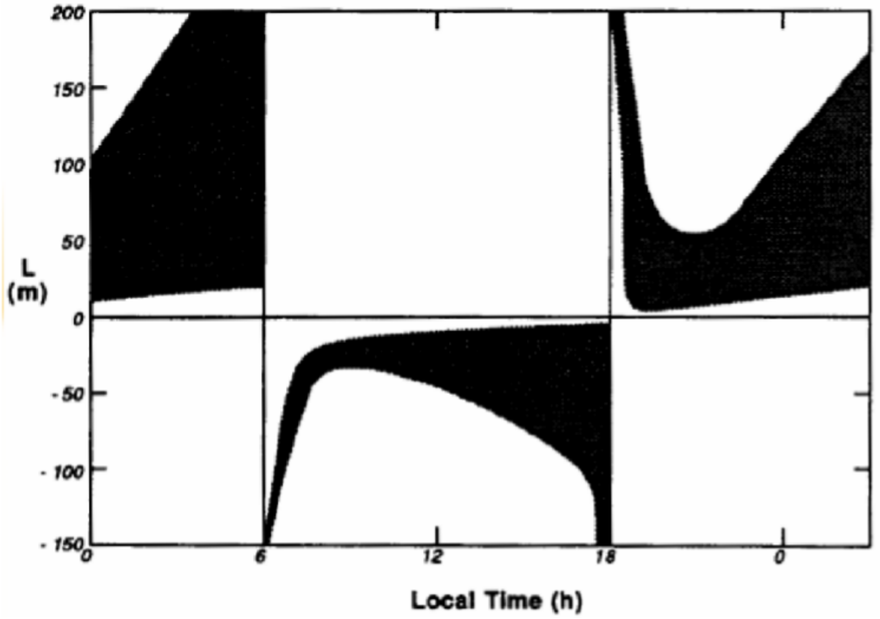

Figure 2.2: *Typical diurnal evolution of the Obukhov length in the diurnal cycle. There are positive values of L at night and negative ones during daytime (Stull, 1988).*

stratification at night and convective conditions during daytime. It can be seen that in a nocturnal stable layer the Obukhov length is positive and during daytime, positive buoyancy processes cause negative values of L.

2.5. Vertical profile for neutral stratification

In order to define the vertical profiles of $\overline{u}$ and $\overline{\theta}$ for neutral stratification, the K-theory is necessary. This theory relates the turbulent flux and the vertical gradient of a variable with a turbulent diffusion coefficient (Foken, 2006). For the turbulent momentum and heat fluxes, this assumption leads to the equations:

$$\overline{w'u'} = -K_M \frac{\partial \overline{u}}{\partial z} \tag{2.16}$$

$$\overline{w'\theta'} = -K_H \frac{\partial \overline{\theta}}{\partial z}, \tag{2.17}$$

where K_M and K_H are the diffusion coefficient of momentum and heat, respectively. In a neutral stratification there is the possibility to express the diffusion coefficient of momentum on the basis of the mixing length theory (Etling, 2008):

$$K_M = \kappa \cdot z \cdot u_*. \tag{2.18}$$

By inserting this definition into the equations (2.16) and (2.17) and considering the relationship given by the turbulent Prandtl number $\mathrm{Pr}_t = K_M/K_H$, the fluxes for momentum and temperature take the following form:

$$\overline{w'u'} = -\kappa \cdot z \cdot u_* \frac{\partial \overline{u}}{\partial z} \tag{2.19}$$

$$\overline{w'\theta'} = -\frac{\kappa}{\mathrm{Pr}_t} \cdot z \cdot u_* \frac{\partial \overline{\theta}}{\partial z}. \tag{2.20}$$

The integration of equation (2.19) for momentum from z_0 until the height z with the boundary condition $u(z_0) = 0$ leads to the logarithmic wind profile:

$$\overline{u}(z) = \frac{u_*}{\kappa} \ln\left(\frac{z}{z_0}\right). \tag{2.21}$$

The integration constant z_0 depends on the surface roughness and is therefore called aerodynamic roughness length. The integration of equation (2.20) is done similarly by using a roughness temperature z_{0T} (Foken, 2006):

$$\overline{\theta}(z) = \frac{\vartheta_*}{\kappa} \ln \frac{z}{z_{0T}} + \overline{\theta}(z_{0T}). \tag{2.22}$$

The scaling temperature ϑ_* is defined as the negative ratio of the turbulent heat flux $\overline{w'\theta'}$ to the friction velocity u_*:

$$\vartheta_* = -\frac{\overline{w'\theta'}}{u_*}. \tag{2.23}$$

In theory, the roughness temperature is the height in which the surface temperature is nearly reached. Since there are large temperature gradients near the surface, it is not possible to find this height. For this reason, z_{0T} is assumed as 10 % of the roughness length z_0 (Foken, 2006). Under neutral stratified conditions, the potential temperature does not change with height and therefore the surface sensible turbulent heat flux $(\overline{w'\theta'})_0$ is zero. In equation (2.22) this leads to a constant potential temperature $\theta(z_{0T})$ with height which is consistent with the definition of neutral stratification.

2.6. Monin-Obukhov similarity theory

Figure 2.3 shows the wind profiles for neutral and non neutral stratifications. The typical wind speeds for each stratification are plotted versus the logarithmic height. It can be seen that the wind profiles for stable and unstable stratification do not follow the logarithmic wind profile. This means equation (2.21) is not valid for non neutral conditions. This led to the suggestion that the stability has to be inserted into the model for the vertical wind profile (Liljequist and Cehak, 2007). For the vertical temperature profile, an equivalent assumption applies. A model for these gradients was developed by the

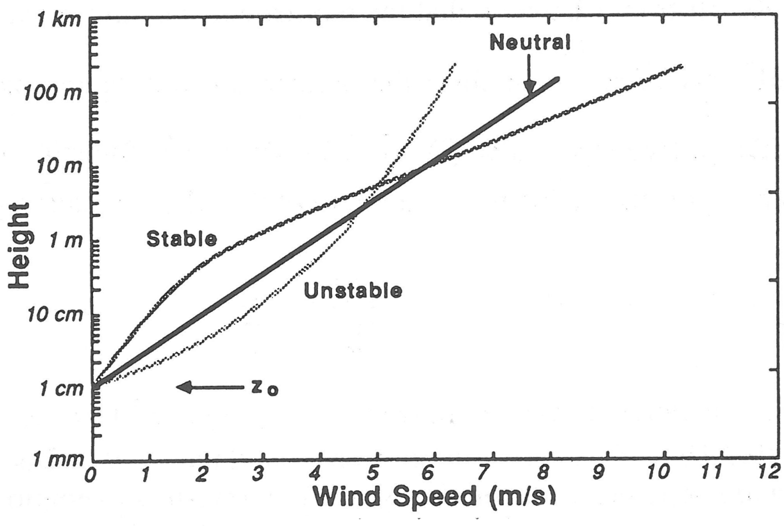

Figure 2.3: *Mean wind at different levels for the non stable case, the neutral case and stable stratification. It is visible that the profiles for stable and unstable stratification diverge from the neutral case (from Oke, 1988).*

need of a flux-gradient relationship for an atmosphere with temperature inhomogeneity. This need is based on the existence of the essential influence of the stratification on the development of turbulence which is obvious in the Richardson number. Monin and Obukhov (1954) developed a flux-gradient relationship for the non neutral stratification which is known as Monin-Obukov (M-O) similarity theory. Since the formula for the wind and the temperature gradients in non neutral conditions cannot be derived directly from the basic governing equations, they used dimensional analysis and the Buckingham Pi Theorem to reach an empirical formulation.

2.6.1. Buckingham Pi Theorem

The main requirement for the use of the Buckingham Pi theorem is to find a list which contains all governing parameters for the dependent variable (Wyngaard, 2010), in this special case the temperature gradient. In this step two errors can be made. The first one is that more variables are selected than necessary. So result will be that there is no change of the other dimensionless groups with respect to the variable that is irrelevant. The second error is that an important dependent variable is not included in the list of governing parameters. The result will be that there is large scatter or no repeatable patterns between the dimensionless groups (Stull, 1988).
With the initial point that all governing parameters $m-1$ of a dependent variable are found, and these have n dimensions, then it is possible to form $m-n$ independent dimensionless quantities out of the governing parameters. Additionally the theorem predicts that these $m-n$ independent dimensionless parameters are functionally related (Wyngaard, 2010).

2.6.2. M-O similarity Theory

In the case of stationary, horizontally homogeneous, thermally stratified flow in motion at a given point in space, the governing parameters of the mean wind gradient are: i) the measurement height z, ii) the friction velocity u_* and iii) the Obukhov length L (Wyngaard, 2010; Barenblatt and Monin, 1979). The boundary layer depth h is not included since its influence on the turbulence at the surface-layer can be neglected. Furthermore, molecular diffusivites and the roughness length z_0 are excluded as governing parameters. The exclusion of z_0 as a dependent parameter leads to the restriction that M-O similarity can only be applied for measurement heights $z \gg z_0$ (Wyngaard, 2010). This means that there are $n = 2$ dimensions and $m = 3 + 1$ dependent parameters: three governing parameters and the mean wind gradient. Thus, there are $m - n = 2$ independent dimensionless quantities which are functionally related. As one of the two independent dimensionless parameters a dimensionless gradient is formed and for the other one, the dimensionless height ς is chosen which was already introduced in section 2.4. This leads to the formulation:

$$\frac{\partial \bar{u}}{\partial z}\frac{\kappa z}{u_*} = \Phi_M(\varsigma), \tag{2.24}$$

where the dimensionless gradient of wind speed is functionally related to ς. Like the Obukhov length and the Richardson number, the dimensionless height is a stability parameter. It takes negative values for unstable stratification, positive ones for stable conditions and is zero for neutral stratification. The von Kármán constant κ has to be introduced into the equation in order to reach the logarithmic wind profile in neutral conditions (Kramm and Herbert, 2009). This means that the von Kármán constant is defined such that $\Phi_M(0) = 1$ (Busch, 1973). The dimensionless gradient for temperature looks similar to equation (2.24):

$$\frac{\partial \overline{\theta}}{\partial z}\frac{\kappa}{\mathrm{Pr}_t}\frac{z}{\vartheta_*} = \Phi_H(\varsigma). \tag{2.25}$$

Here the turbulent heat flux $(\overline{w'T'})_0$ has to be considered as fifth governing parameter and the temperature as third dimension, which again leads to $5 - 3 = 2$ dimensionless independent variables. Since for neutral stratification equation (2.23) has to be reached, also a value of $\Phi_H(0) = 1$ is predicted. To reach this, κ has to be factorized by the turbulent Prandtl number in the dimensionless gradient of temperature (Foken and Skeib, 1983). The functions Φ_M and Φ_H are predicted to be universal. This means they are the same in all locally homogeneous, quasi-steady surface layers (Wyngaard, 2010).
It is also possible to formulate the dimensionless gradient of moisture or a conserved scalar constituent in a similar way as the dimensionless gradient of temperature (Foken, 2006).

2.6.3. State of research

The universal functions cannot be derived mathematically. This means there is the need to determine them experimentally in the field. One of the most famous experiments with respect to the M-O similarity theory is the KANSAS experiment. Businger et al. (1971) analysed temperature and wind profiles over a wide range of stability conditions with different expressions for Φ_M. One of the formula used and confirmed by them was the O'KEYPS-equation (Businger, 1988; Panofsky, 1963):

$$[\Phi_M(\varsigma)]^4 - \gamma \cdot \varsigma \cdot [\Phi_M(\varsigma)]^3 = 1, \tag{2.26}$$

where γ is an independent parameter which has to be estimated experimentally. For unstable stratification ($\varsigma < 0$), solutions of this formula have the form:

$$\Phi_M = (1 + \gamma_1 \cdot \varsigma)^{-1/4}. \tag{2.27}$$

For the stable case ($\varsigma > 0$), the universal functions develop mainly linear:

$$\Phi_M = 1 + \gamma_2 \cdot \varsigma. \tag{2.28}$$

γ_1 and γ_2 are independent parameters which have to be estimated experimentally. In order to get the similar expressions for the universal function of temperature, one can use the following relations (Foken, 2006):

$$\Phi_H \approx \Phi_M^2 \qquad \text{for} \qquad \varsigma < 0 \tag{2.29}$$

$$\Phi_H \approx \Phi_M \qquad \text{for} \qquad \varsigma \geq 0 \tag{2.30}$$

In the following, the turbulent Prandtl number will be included into the formulation for the universal function Φ_H. This means the relationship between the dimensionless gradient for temperature and the universal function is:

$$\frac{\partial \overline{T}}{\partial z}\frac{\kappa z}{\vartheta_*} = \begin{cases} \mathrm{Pr}_t \cdot (1 + \gamma_1 \frac{z}{L})^{-1/2} & \text{for } \varsigma < 0 \\ \mathrm{Pr}_t \cdot (1 + \gamma_2 \frac{z}{L}) & \text{for } \varsigma > 0 \end{cases} \tag{2.31}$$

The procedure in order to reach the universal functions is illustrated on the data from the KANSAS experiment. Figure 2.4 shows the dimensionless gradients of temperature and wind speed plotted against ς. It can be seen that there is a functional relationship between the dimensionless gradient plotted on the y-axis to the dimensionless height on the x-axis. This functional relationship is generally expressed by equations (2.27) and (2.28) for wind speed and equations (2.31) for temperature, respectively. This means the functions are fitted by the method of least squares in the data points in order to find the values for γ_1 and γ_2. The γ values are not the same for the universal function of wind speed and temperature, although they are labelled equal here. The found formulations of Φ_M and Φ_H are listed in table 2.1 and are labelled with $\Phi_{M,K,\mathrm{org}}$ and $\Phi_{H,K,\mathrm{org}}$. In order to get the von Kármán constant, an analysis for near neutral conditions ($|\varsigma| < 0.1$)

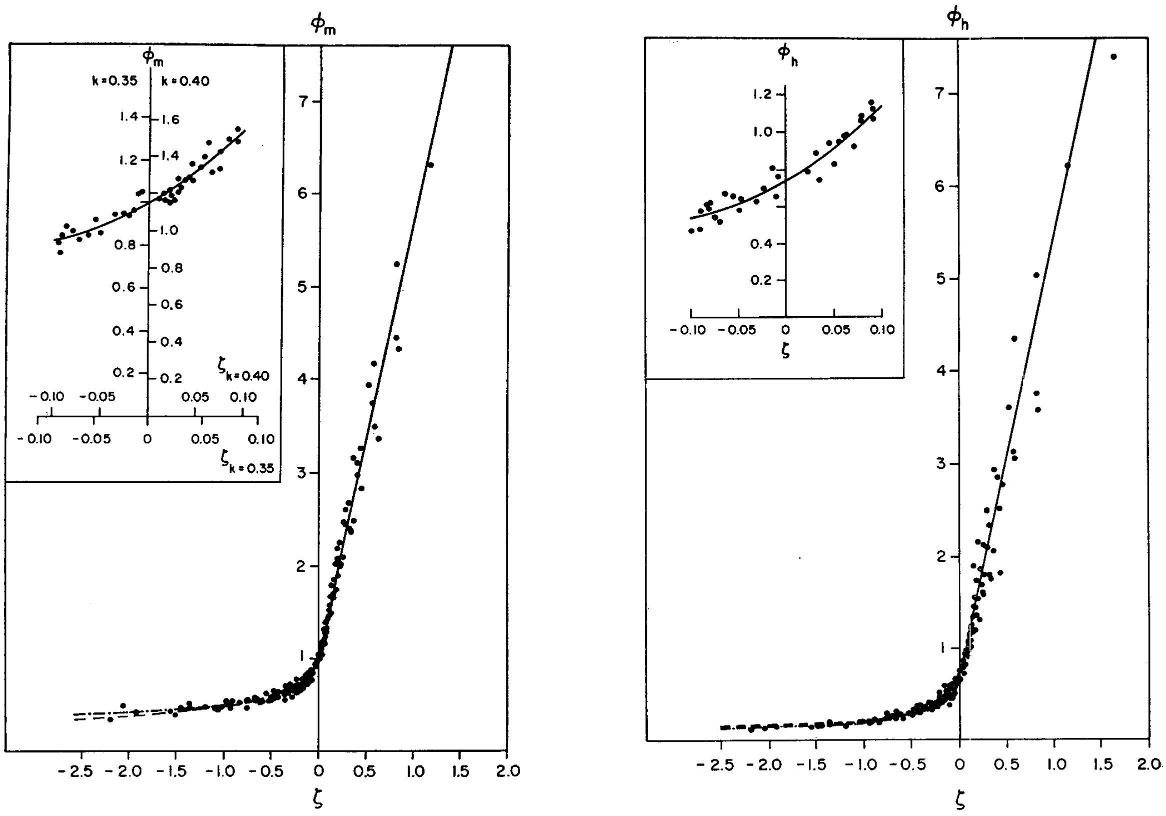

Figure 2.4: *Dimensionless profiles of wind speed Φ_M and temperature Φ_H plotted against the dimensionless height ς. Also the fitted curve is included and analysis of the near neutral range $|\varsigma| < 0.1$. Several interpolation formulas were used which all gives excellent fits to the wind and temperature profiles (Businger et al., 1971).*

was made, also plotted in figure 2.4. The value of κ is chosen so that $\Phi_M(0) = 1$ is fulfilled. The same is done for the universal functions of temperature in order to find the turbulent Prandtl number. With equation (2.31), Pr_t is reached for $\Phi_H(0)$. In the KANSAS experiment, $\kappa = 0.35$ and $\mathrm{Pr}_t = 0.74$ were found.

Although Φ_H and Φ_M are called universal functions, there were remaining differences in the γ-values which were predicted in various experiments. Additionally, different von Kármán constants and turbulent Prandtl numbers were found. The range of κ, for example, varies in literature from 0.35 to 0.41. Högström (1985) states that κ has to be a constant with a value close to 0.4. This assumption is supported by laboratory wind tunnel tests (Högström, 1985).

There are several papers which compare these various universal functions. Yaglom (1977) was the first who corrected the universal functions to the same values of κ and Pr_t in order to make them comparable. An important mention must be done for the work of Högström (1988). He predicted that the variation in the von Kármán constant and the turbulent Prandtl number are systematic deviations due to instrumental shortcomings and do not reflect real differences. Therefore, an experiment was undertaken where great

	κ	unstable	stable
$\Phi_{M,K,\mathrm{org}}$	0.35	$(1-15\varsigma)^{-1/4}$	$1+4.7\varsigma$
$\Phi_{H,K,\mathrm{org}}$		$0.74\cdot(1-9\varsigma)^{-1/2}$	$0.74\cdot(1+6.3\varsigma)$
$\Phi_{M,K}$	0.4	$(1-19.3\varsigma)^{-1/4}$	$1+6.0\varsigma$
$\Phi_{H,K}$		$0.95\cdot(1-11.6\varsigma)^{1/2}$	$0.95\cdot(1+8.2\varsigma)$

Table 2.1: *Universal functions from the KANSAS experiment $\Phi_{M,K,org}$,$\Phi_{H,K,org}$ (Businger et al., 1971) and the functions modified by Högström (1988) $\Phi_{M,K}$,$\Phi_{H,K}$.*

care was taken to remove any measuring errors. In this field study a von Kármán constant of 0.4±0.01 and a turbulent Prandtl number of 0.95±0.04 were derived. In order to make all expressions for Φ_M and Φ_H which appeared in literature comparable, he modified the fluxes in accordance with the following assumptions: $\kappa = 0.4$, $\Phi_H(0) = 0.95$. This modification was legitimated considering that incomplete correction of flow distortion was made in the previous studies. This flow induced distortion causes systematic errors in the fluxes (Högström, 1982; Wyngaard, 1981). Therefore the fluxes in the different expressions of the universal functions were multiplied with 'correction factors' in order to reach the above mentioned assumptions. The functions of the KANSAS experiment and modified by Högström (1988) are listed in table 2.1. They will be further described as $\Phi_{M,K}$ and $\Phi_{H,K}$. Other functions which were modified by Högström (1988) are listed in table A.4 and A.5. Högström (1996) summarized the possible reasons for the remaining differences in the various formulations, after he homogenised all data sets with the before mentioned 'normalization procedure':

1. Statistical uncertainty in the individual averaging time periods
2. Systematic instrumental inaccuracy not adequately corrected by his 'correction procedure'
3. Inadequate upwind fetch
4. Systematic errors due to inadequate sampling
5. Limitations of the M-O similarity theory

Errors caused by the first three categories were responsible for differences in the compared functions in the order of ±10 %. In the last category, Högström (1996) counted the limitation of the M-O similarity in very stable conditions. Foken (2006) called the deviation of the M-O similarity for $\varsigma > 1$ 'z-less scaling'. In very stable conditions, the turbulence becomes so sporadic that the size of the eddies is no longer dependent on the distance of the measurement instrument to the earth's surface. Thus, the universal functions become almost constant. This assumption is included in figure 2.5 as 'modified' universal function. The figure also shows the typical development of Φ_M and Φ_H. Wyngaard (2010) took a step further and predicted that there are also limitations for

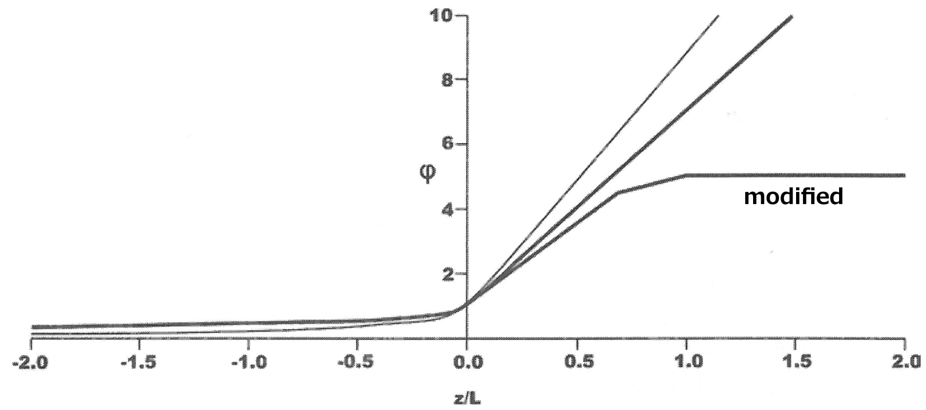

Figure 2.5: *Typical developing of universal function for wind speed (bold line) and temperature (thin line). The curve labelled with 'modified' reflect the assumption of an almost constant universal function for very stable stratification (Foken, 2006).*

the very unstable case. For $\varsigma < -1$ there might be a height in which the direct effects of shear production become unimportant compared to buoyant production. The reason is that in the surface layer the buoyant production of TKE is essentially independent of height, while the rate of shear production decreases with height.
It was already mentioned in section 2.6.2 that there is also a vertical limitation which states that M-O similarity is only valid for $z/z_0 \gg 1$ (Wyngaard, 2010). In this content, Garratt (1980, 1983) investigated the dimensionless vertical profiles of wind and temperature over a flat, tree covered terrain. He found a lower height limit z_* for the universal functions, where z_* is the depth of the transition layer. This transition layer lays between the intertial and the roughness layer. Within this layer, a modified function depending on the dimensionless height and the transition layer depth should be considered.

3. Description of the experimental site and instrumentation

All data used in this bachelor thesis were sampled during the BLLAST (Boundary Layer Late Afternoon and Sunset Turbulence) campaign which took place from 14th June until 8th July 2011 in Lannemezan, France. The objective of this campaign was to reach a better comprehension of the physical processes that control the late afternoon and the early morning transition (ExPlans, 2011). However, this thesis does not deal with these transition periods. The main reason is that these time periods come along with fast changes of the atmospheric parameters whereas for M-O similarity theory steady state conditions are assumed. Furthermore, there were measurement issues during the transition times which will be described in section 3.2.1.

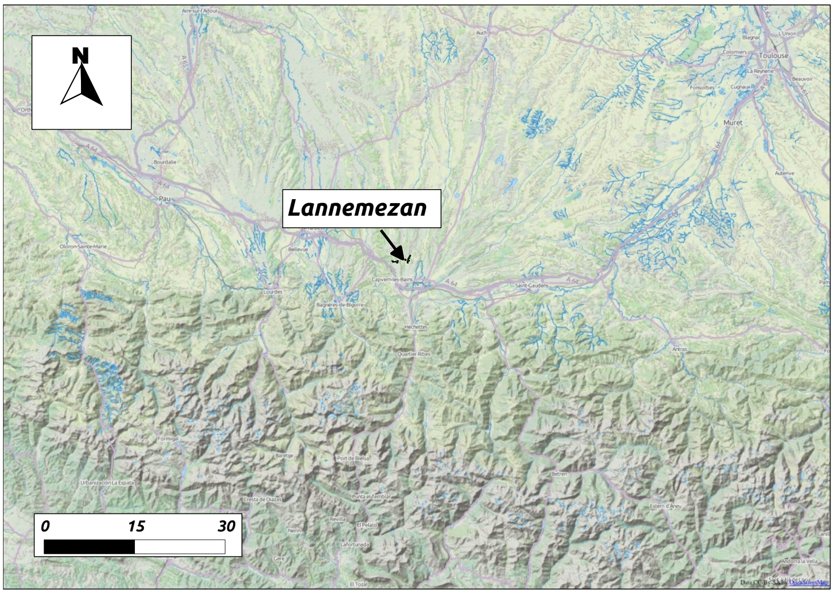

Figure 3.1: *Map of the topography around Lannemezan. The city of Lannemezan is located on the northern foothill of the Pyrenees mountains on a plateau of about* 200 km^2*. It is visible that there are south-north oriented valleys at the south of Lannemezan. The map is taken from* openstreetmap*. The scale is given in km.*

3.1. The site

The area frame of the BLLAST field campaign described in this section is taken from the experimental plans of the campaign (ExPlans, 2011). The field campaign took place on the plateau of Lannemezan at the northern foothills of the Pyrenees mountains. The plateau spans an area of about 200 km^2 and is aligned with the south-north oriented valleys which are located in the mountain range. Figure 3.1 shows a topographic map of the area around Lannemezan in which its position in the north of the Pyrenees mountains is indicated. The geographical configuration is responsible for a particular mesoscale wind circulation under fair weather conditions. These low level wind patterns will be used in the selection of adequate time periods in section 4.1. The description of the wind system has been addressed by Jimenez and Cuxart (2012) through a numerical simulation of this area.

Figure 3.2 shows the wind speed and direction from the 1st July at noon until next day noon. The time is given in coordinated universal time (UTC). This data are taken as an example for a day with clear skies and weak synoptic pressure gradients (Jimenez and Cuxart, 2012). It can be seen that the main wind direction during daytime is north (50 to 300 °) whereas at night, wind with a southern component (140 to 200 °) dominates. In figure 4.2a a histogram of the wind direction for this 24 hours time period is plotted. The figure also points out the predominance of these two wind directions. Northern wind comes from the inland of France. This means there has to be a formation of

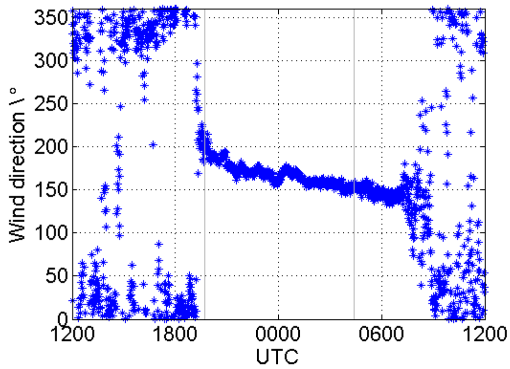

(a)

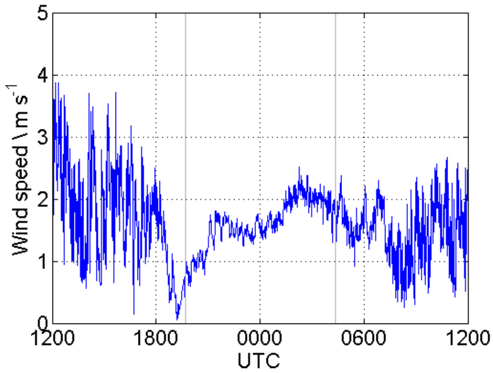

(b)

Figure 3.2: *Wind speed and wind direction for 1st July noon to the next day noon. The vertical grey lines indicate sunset and sunrise. This day is taken as an example for the behaviour of the wind circulation without a synoptic influence. It can be seen that the main wind direction during daytime is north (50 to* 300 °*), whereas at night the wind is blowing from the south (140 to* 200 °*). A histogram of the wind direction for this time period is given in figure 4.2a.*

a temporary low pressure system above the Pyrenees during daytime. Shortly before sunset, a rotation of the wind field of about 180 ° occurs together with low wind speeds, followed by winds from the mountains into the lowlands. This mesoscale wind system is related to the mountain-plain winds circulation and can be observed best in anticyclonic weather in summer, when large-scale flows are weak (Martinez, 2011). The mountain-plain winds are mainly driven by horizontal temperature differences between the air over the Pyrenees and the air over the inland of France. The main reason for this is the area of contact between a volume of air and the surface. This area is larger on slopes and so the parcel of air can be heated more effectively. The warmer air above the mountains compared to the lowlands causes a pressure gradient which results in winds blowing up the outer slopes during the day. For Lannemezan, this means a wind from the north. At night, the divergence of the long wave radiation flux cools the air close to the surface. This causes a drainage wind from the mountains into the surrounding plains (Stull, 1988). Since the air columns in mountain regions are cooling faster due to their larger area of contact to the surface, the down slope winds are additionally driven by pressure gradients. For Lannemezan, this means wind with a southern component at night. A sketch of the wind circulation for day and night can be seen in figure 3.3.

Beside this mesoscale circulation other characteristics of the wind speed and wind directions can be observed. It can also be seen in figure 3.2 that the fluctuations of the wind speed and direction during daytime are much larger than at night. These fluctuations can be explained by the convective conditions during daytime. Air masses above the surface are heated by the underlying ground and the air begins to rise. Since figure 3.2 shows the situation for a cloudless day with high insolation, the buoyancy

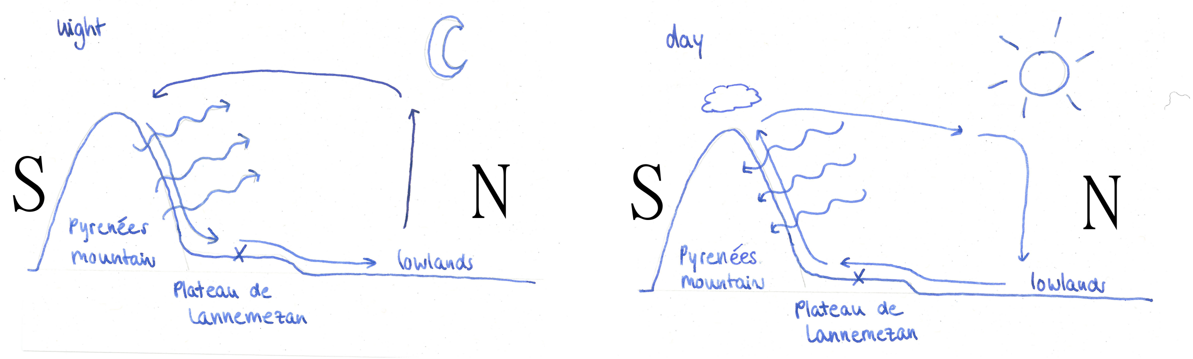

Figure 3.3: *Sketch of the mesoscale wind system in the area of Lannemezan. During daytime the air above the slopes heats more compared to the lowlands. This causes wind from the lowlands during daytime. At night the air cools due to radiative emission and therefore a flow into the lowlands is accelerated by gravity and pressure-gradient forces.*

is large, too. At night, the fluctuations are dumped by the predominance of stable stratification. A point which is visible in the development of the wind direction at night are changes in the main wind direction for short time periods. Examples for this are the peaks in figure 3.2a around 0000 UTC. These irregularities in the wind direction could be explained by the circumstance that there is one very big valley in the south of Lannemezan and several smaller ones. This means, it is possible that most of the drainage flows are allocated to the big valley, whereas flows from other valleys shortly influences the mean flow. This irregularities of the mean wind direction at night will also be considered in the selection of the time periods in section 4.1.
Beside this meso-scale consideration of the measurement site, it is also important to assess the characteristics of the nearby environment of the sensors. During BLLAST campaign there were two super sites which had a spatial distance of about 5 km. Super site one served for the measurement of vertical structure and super site two for spatial heterogeneity. In both sites the surface was mainly covered by heterogeneous vegetation: grasslands, meadows, crops and forest. These two super sites were again divided into several sub sites. All measurement data used in this bachelor thesis were sampled at the sub site 'micro scale surface heterogeneity' of super site one. This site was settled west of Lannemezan and had the shape of a square with a side length of about 150 m. The location and the shape of the site can be seen in figure 3.4. It is also visible in this map that there is a forest with a distance less than 200 m to the east of the measurement site. The name of the site has already introduced that the surface is covered by small bushes, grass and small puddles (Martinez et al., 2012). However, for the present work it is assumed that the site is horizontal homogeneous.

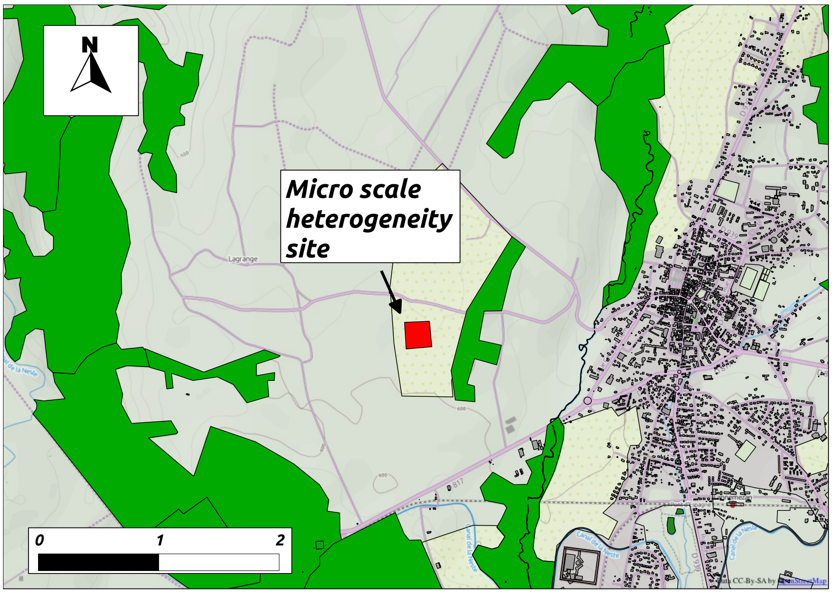

Figure 3.4: *Map of the area around the measurement field. The micro scale heterogeneity site is marked inside the map as a red rectangle and the areas covered with trees are marked in green. It is visible that the distance to the forest to the east of the measurement site is less than* 200 m*. That means for wind blowing from this direction not necessarily a uniform fetch is given. The map is taken from* openstreetmap *, whereupon the measurement site is mapped with* QGIS *and its coordinates are taken from a satellite picture of* google earth.*The scale is given in km.*

3.2. Instrumentation

As already mentioned, the whole data which are used for the assessment of the M-O similarity theory was sampled in a site which spans an area of about 2.25 km^2. The data are taken from an eddy covariance station, a 8−m tower, a portable station and a 2-m mast.
The eddy covariance station was installed by the University of Bergen and was equipped with a three dimensional sonic anemometer and with a Licor. For the calculation of the fluxes it is necessary to have an instrument which is able to measure wind and temperature fluctuations at high frequency. For this reason, the sonic anemometer and the Licor measured the turbulent wind and temperature with a time resolution of 10 Hz. The measurement height was 1.95 m AGL, wherefore the fluxes measured at the eddy covariance station will be taken as the turbulent surface fluxes.
At the 9 −m mast which was installed by the University of Bergen, several atmospheric parameters were measured in three different heights. There were measurements of wind speed and wind direction, temperature probes and humidity sensors. The atmospheric parameter used in this bachelor thesis are the temperature and the wind speed and direction. These measurements were taken with cup anemometers and wind vanes at 2.1, 5.1 and 8.6 m AGL. The wind direction is used in order to state fair weather conditions and to assess the fetch receptive to its potential disturbance by nearby roughness elements.

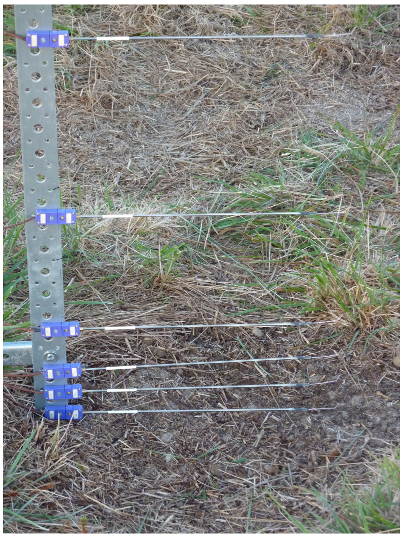

(a)

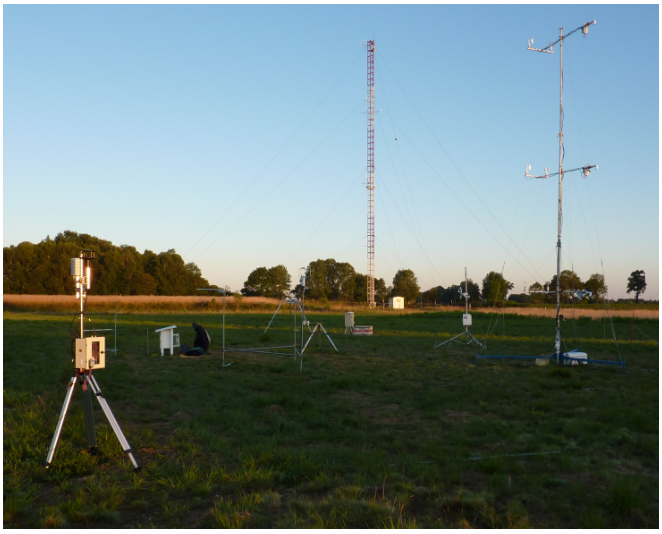

(b)

Figure 3.5: $2-\mathrm{m}$ *mast with the lower six thermocouples in different heights (a). It can be seen that the surface is covered with bare soil, dry and green grass. (b) Overview of the measurement devices at the micro scale heterogeneity site. On the right hand site the* $9-\mathrm{m}$ *tower with measurement instruments in three different levels is visible. On the left site the portable station of the UIB is located. In the background a* $60-\mathrm{m}$ *tower can be seen which was installed in the north western corner of the site.*

The wind speed is used to analyse the wind profile.
Additionally to this, wind measurements from the portable station of the University of the Balearic Islands (UIB) is used. The wind speed and wind direction were measured with a two dimensional sonic anemometer. Since no continuous measurement of this station is available, the data are mainly used to verify the wind data from the $9-\mathrm{m}$ mast. Furthermore the portable station was equipped with a platinum resistance temperature detector (PRT). Since the temperature measured by this probe was tested and verified several times before the BLLAST field campaign, it will be taken as reference temperature in order to assess other temperature measurements. The whole measurement site is shown in figure 3.5b.

3.2.1. Thermocouples

The focus of the data analysis is taken on the lowest 2 m of the ABL. This means, profile measurements of the temperature within this height are essential. These measurements were taken by a $2-\mathrm{m}$ mast which was equipped by eight thermocouples. The thermocouples were installed on branches in different heights on the mast that are listed in table 3.1. Figure 3.5a shows a picture of the lower six thermocouples. It can be seen that the lowest thermocouples are installed within the vegetation. The thermocouples measured the temperature with a sampling rate of 10 Hz, whereupon it is assumed that the real resolution is about 1 Hz. During the field campaign there were problems referring to the

#	1	2	3	4	5	6	7	8
Height AGL \m	0.015	0.045	0.075	0.14	0.30	0.515	1.045	1.92

Table 3.1: *Heights above ground level (AGL) for the eight thermocouples.*

thermocouple measurements. Since the temperature profile is used for the calculation of the dimensionless gradients, these problems have to be assessed in detail. In Figure 3.6 the temperatures measured by the thermocouples are compared to the temperature sampled by the portable station. The temperatures are plotted over 24 hours from noon to noon. It can be seen that around sunrise, the temperature measured by both sensors increases at different rates. The thermocouples show a sudden drop up to 3 K shortly after sunrise before increasing again two hours later. This anomaly in the behaviour of the air temperature recorded by the thermocouples after sunrise was measured several days along the campaign, but it was never reproduced by the portable station. The different measurement conditions between the two types of sensors can be a reason for this discrepancy. The PRT of the portable station was mounted in a radiation shield, while the thermocouples were installed without any protection. Therefore, the measurements of the portable station have been considered as reference value in this bachelor thesis. However, it can not be discarded errors under quiescent or weak wind conditions, when a lack of ventilation could lead to erroneous reading inside the radiation shield. Since this issue is a research topic itself it will not be further discussed in this present work. The mean relative difference for one day between the two temperature probes is up to 16 % when the temperature measured by the PRT is taken as accepted value. In order to find an alternative explanation for the difference it is necessary to understand the operating mode of a thermocouple. Thermocouples consist of two conductors of different materials. In order to measure the air temperature, the thermocouple has to be composed of a reference junction and a measurement junction. If the measurement end of the thermocouple is at a different temperature as the reference end, a voltage potential (U_{th}) is created (CR1000, 2011). The effect that the conductor generates a voltage when it is subjected to a thermal gradient is called the 'Seebeck effect'. The generated voltage is proportional to the temperature difference (ΔT) of the two junctions:

$$U_{\mathrm{th}} = \alpha \cdot \Delta T = \alpha \cdot (T_{\mathrm{wj}} - T_{\mathrm{cj}}), \tag{3.1}$$

where T_{cj} and T_{wj} are the temperatures at the reference (cold junction) and at the measurement junctions (warm junction), respectively. The constant of proportionality α is the difference between the Seebeck coefficient of the two materials. The Seebeck coefficient depends on the material of the conductors and has to be constant over the

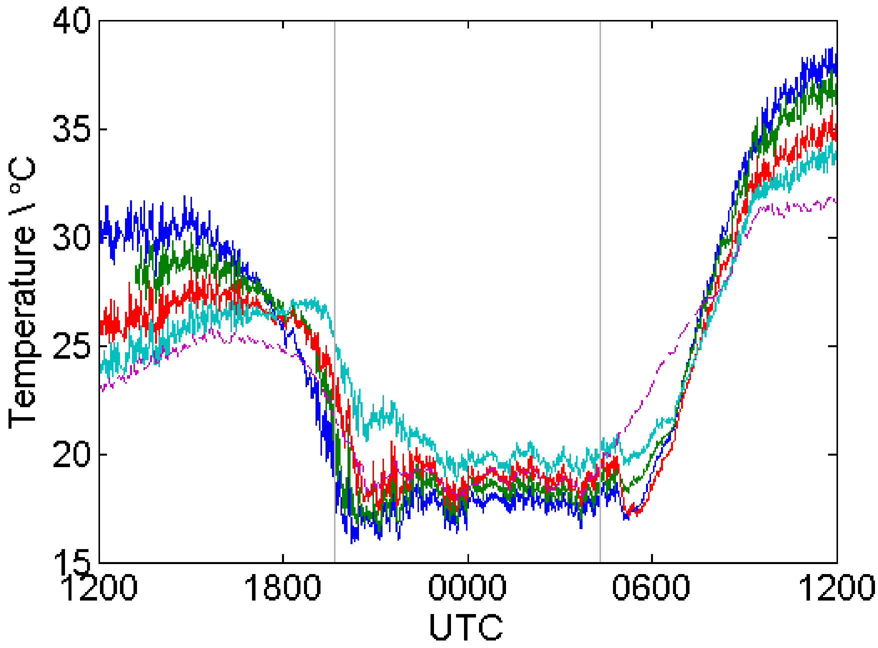

Figure 3.6: *Temperatures of thermocouple #1 (—), #3 (—), #5 (—), #8 (—) and the temperature probe measured at the portable station (PRT) (– –). The data are plotted from noon of the 25th June until noon of the following day. During most of the 24 hours the discrepancy between the thermocouples and the temperature measured by the portable station is small except for the time period shortly after sunrise. The highest thermocouple (#8) has nearly the same values than the temperature measured at the portable station. Since both probes are mounted approximately at* 2 m *height, the small discrepancy is interpreted as a sign for the accuracy of the thermocouple measurement.*

measured temperature range. With the output voltage U_{th} as the measured variable the temperature at the reference junction has to be known to calculate the air temperature. The thermocouples used in this experiment are of type E, so the two different materials are chromel and constantan. Each of the eight thermocouples were connected to an extension cable which ends at a box with a plug for each one. A black plastic bag covered the plugs to protect them from rain. The installation is shown in Figure 3.7.
The extension cables were special ones for thermocouples which consist of the same material and extend the thermocouples without influencing the output voltage. That means that the reference junction moves from the instrument to the other end of the extension cable. The plugs for the sensors are connected to a multiplexer which is in direct contact with the datalogger. Both the multiplexer and the datalogger are in an enclosure box nearby the plugs. The cables from the plugs to the multiplexer are made of different material than the thermocouples and therefore do not have an influence to the thermal voltage. The multiplexer is, like the extension cables, made for thermocou-

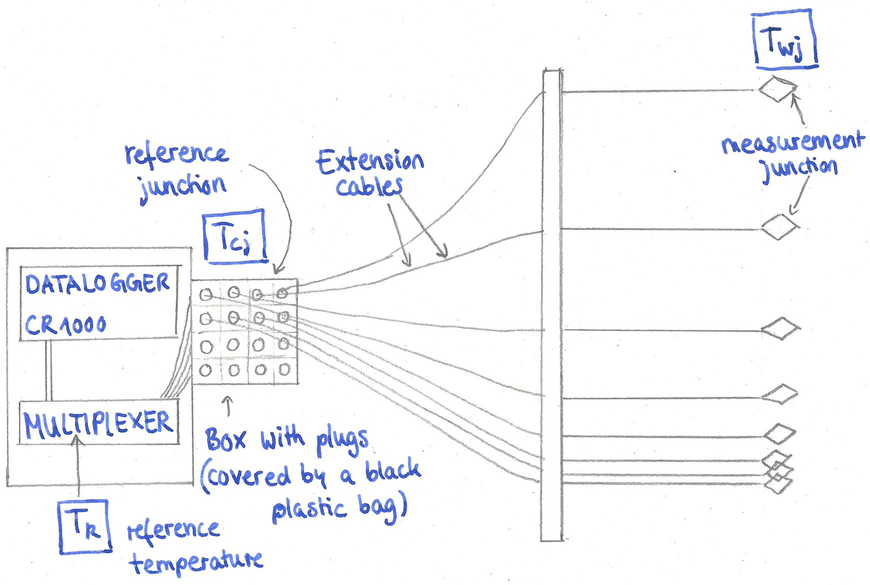

Figure 3.7: *Sketch of the installation of the thermocouples in the field. T_{wj} is the temperature at the measurement junction. The temperature of the reference junction T_{cj} is taken on the box with the plugs. These are connected to a multiplexer in a box nearby were the reference temperature T_R is measured.*

ples and contains a resistance temperature device to measure the reference temperature (T_R). Since the voltage U_{th} is measured between the reference junction T_{cj} and the measurement junction T_{wj}, the temperature measured in the multiplexer could only be used for the calculation of the air temperature if it was of same temperature as the reference junction. As the reference temperature and the reference junction are in different boxes there is the possibility of a temperature gradient between both. This gradient reaches its maximum when there is a fast temperature change inside the black plastic bag. Fast change in air temperature happens especially before sunrise and after sunset. If the gradient gets higher and therefore the difference between T_R and T_{cj} becomes larger, there are two possible errors in the interpretation of the output voltage. The first one is an overestimation of U_{th} and the second one an underestimation. A wrong estimation of the voltage leads to the calculation of a wrong air temperature. Figure 3.8 includes the temperature at the portable station, the temperature of the highest thermocouple (T_{wj}) and the reference temperature (T_R) measured by the multiplexer.

This reference temperature T_R was used to calculate the air temperature T_{wj}. However, the 'temperature valley' which starts at approximately 0500 UTC leads to the supposition that the reference temperature is not consistent with the temperature of the reference junction T_{cj}. The reference junction is located at the plug inside a black plastic bag (see figure 3.7). Since black is a good absorber for solar radiation, the air temperature inside the plastic bag increases fast when sunbeams shine on it. Since the

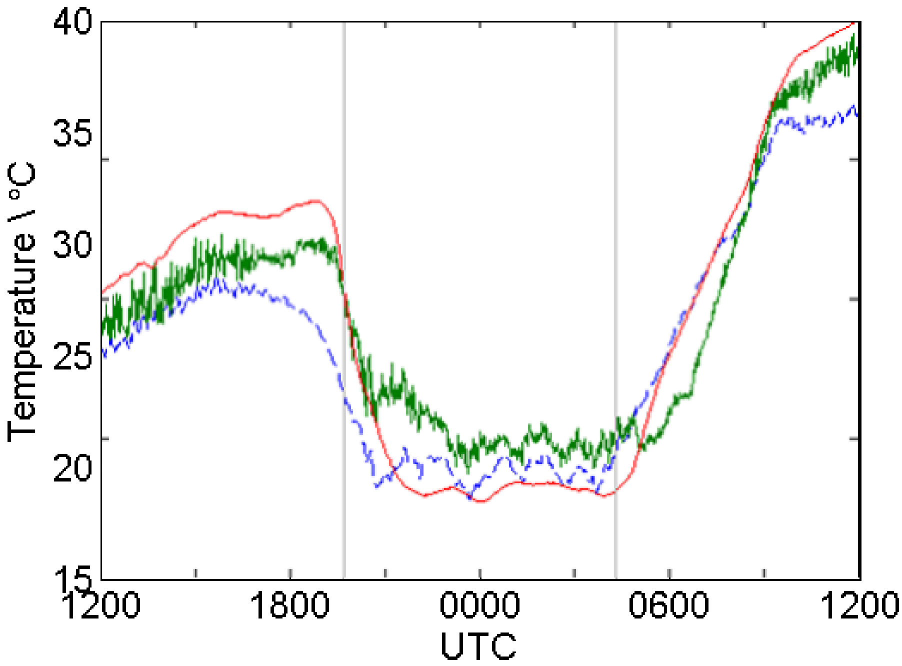

Figure 3.8: *Temperatures of the highest thermocouple (#8)(—), the portable station (—) and the reference temperature (T_R)(—). The data are taken from the 25th June and is plotted for 24 hours starting at noon. The vertical grey lines indicate the time of sunset and sunrise.*

reference temperature measurement occurs in an enclosure box, it could be that the air inside the enclosure box needs more time to get heated by the sun. In this case, the output voltage of the thermocouple (U_{th}) would be underestimated and therefore leads to the calculation of a lower temperature (T_{wj}) than the real value should be. Before sunset the converse phenomena can be observed. The air inside the plastic bag cools faster than the air inside the box. It comes to an overestimation of the output voltage (U_{th}) and therefore to an overestimation of the air temperature (T_{wj}).
In figure 3.9 the difference of thermocouple #8 and the temperature measured by the portable station is plotted. If the temperature measured by the PRT is taken as the true air temperature, the difference is consistent with the bias. This bias is estimated for 15 minute averaged temperature data over ten days, the standard deviation is shown as error bars in the plot. The large errors during transition times can clearly be seen and are consistent with the expected overestimation around sunset and underestimation after sunset. But also outside of these periods the bias never takes a value of zero. This means there has to be a systematic error in the thermocouples.
Since the thermocouples are used for the calculation of the universal functions it is important to correct their measurements. To find a linear function for the correction of the thermocouples, the temperature of the highest thermocouple is plotted versus the temperature sampled by the portable station. Since the systematic error is expected to

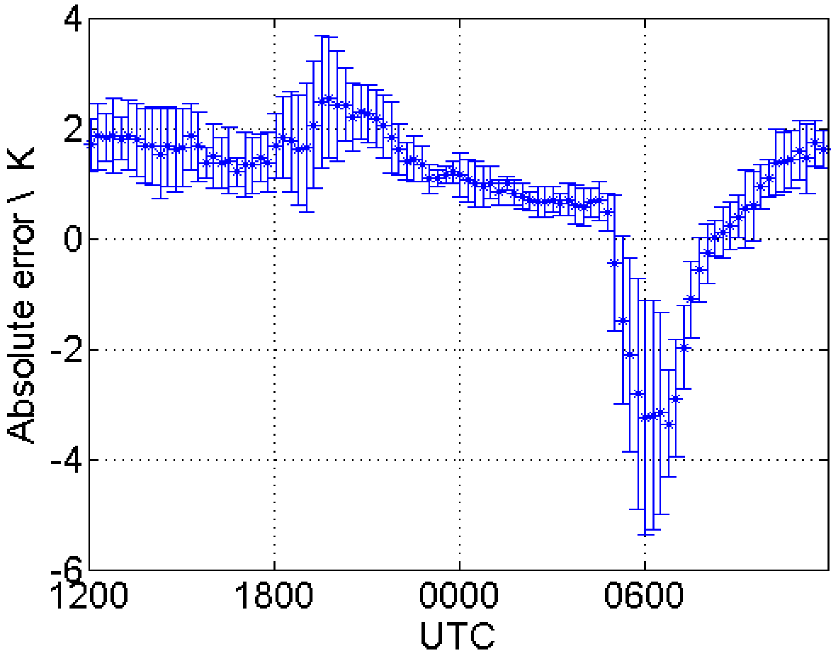

Figure 3.9: *The absolute error of thermocouple #8 relative to the measurement of the portable station is plotted against time. The error is estimated for 15 minute averaged temperature data over ten days.*

be not constant for transition periods, the times periods 1900 to 2300 UTC and 0500 to 0800 UTC are excluded. A linear regression is made in order to find a correction function for the temperature data. The data points and the linear function are plotted in figure 3.10. Since the value for R^2 (see section A.1) is higher than 0.99, it is allowed to use the function directly for correction (Foken, 2006). This means in the current work, the thermocouple temperature data were corrected with:

$$T'_{\mathrm{TC}} = 1.05 \cdot T_{\mathrm{TC}} - 14.0, \tag{3.2}$$

where T'_{TC} is the corrected and T_{TC} the measured air temperature, respectively. The correction function is defined for temperature in Kelvin. Since there is a difference in the measurement height of approximately 10 cm between the highest thermocouple and the portable station, it could be argued that the temperature differences between the two sensors is related to the temperature gradient. There are two arguments against this supposition. The first one is that the differences always have the same sign. This means, that the thermocouples always show a higher temperature than the PRT, even during daytime. The second can be taken from the change of temperature with height which is estimated in section 4.2. The function there is used to extrapolate the temperature in 2 m heights. It was found, that the temperature gradients in this height are already so small that the temperature difference between 1.92 m and 2 m can be neglected.

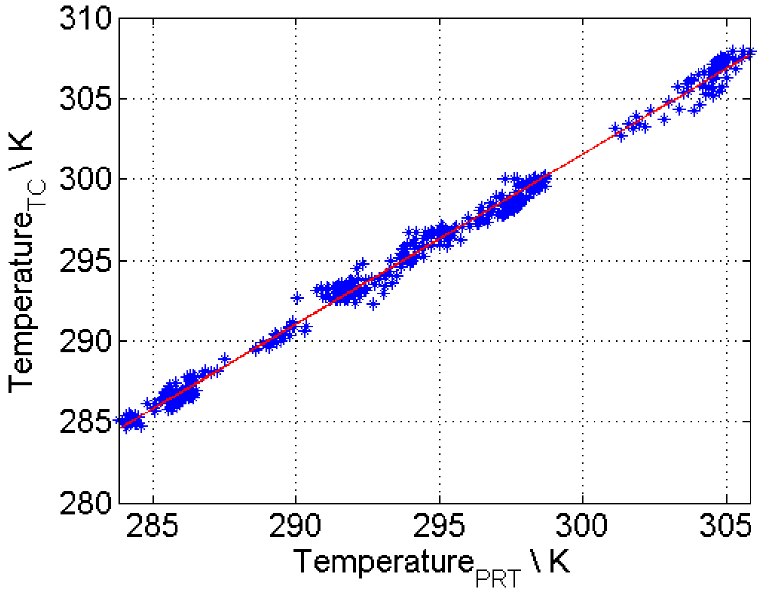

Figure 3.10: *Temperature measured by thermocouple #8 (Thermocouple$_{TC}$) versus the temperature measured by the portable station (Thermocouple$_{PRT}$)(*). A linear function is fitted through the data by the method of least squares. This function $T'_{TC} = 1.05 \cdot T_{TC} - 14.0$ (—) is used to correct the thermocouple data*

4. Implementation to the data

Since a lot of different variables are used for the calculation of the universal functions, the data processing took a quite big effort in the implementation to the data. A rough overview of the data handling shall be given here. The data processing was done with the software MATLAB. The data were given in three different formates. The first one was the data of the UIB, the second one came from the University of Bergen and the last one from the University of Wageningen.
The data of the UIB are organized in single .dat files. Each file contains one minute data of an atmospheric parameter for a time period of 24 hours. These time periods start at noon of the day and contain data until at least 1159 UTC of the next day. Since data were not available for full 24 hours for each day, the length of the columns containing the data were not homogeneous. In order to simplify the further work with these data, all files where rewritten in two files with continuous times. One of them contains the data of the thermocouples and the other one the rest of the used parameters of the UIB. Although the data of the $9-\mathrm{m}$ mast and the data of the eddy covariance station were both sampled by the University of Bergen, their data organisation differs. The reason for this is that the eddy covariance data were processed by members of the University of Wageningen who wanted to process the data of all eddy covariance stations installed during BLLAST campaign in the same way.
The files for the eddy covariance station already contain calculated fluxes. Since for

the calculation of the covariance between two variables the average of these variables is necessary, three files with different averaging time periods are available. The averaging periods are 5, 10 and 30 minutes.
The data of the $9-\mathrm{m}$ mast are available as a continuous file with 1 minute averaged data.

4.1. Selection of time periods

In the derivation of the universal functions, horizontal homogeneity and steady state are applied. For this reason criteria has to be found to assume both. There are two requirements on the averaging time period. The first one is that steady-state can be assumed and therefore the time intervals should have a minimum width in which the average temperature does not change with time ($\partial\bar{\theta}/\partial t = 0$). Secondly, the time periods have to be long enough to include all eddy sizes. For this reason Wyngaard (2010) introduced a time scale of unsteadiness τ_u to estimate the minimum width of the averaging time period. This parameter depends on the height of the sensor and the friction velocity. For the calculation of this parameter, the raw data of the turbulent wind and temperature are necessary which were not available for this bachelor thesis. Since in literature no appropriate method is found to determine a time period of steadiness quantitatively, 15 and 30 minutes time periods are used and compared. This is done since the statistical uncertainty in the individual averaging intervals were listed as one reason for the differences between the universal functions through literature (see section 2.6.3, Högström (1988)).
Another step to ensure steady state is the exclusion of the time periods of late afternoon and early morning transitions. Since these transition periods are connected with rapid time changes (ExPlans, 2011), steady state conditions can not be assumed. This means that data are excluded from 1900 to 2300 UTC and 0500 to 0800 UTC. These ranges seem unusual for transition periods. The reason why these periods are chosen has its origin in the large differences between the temperature measured by the highest thermocouple and the PRT around these time periods (see section 3.2.1).
To state horizontal homogeneity, Wyngaard (2010) introduced a length scale of inhomogeneity L_x:

$$L_x \gg \frac{\bar{u}}{u_*} z, \tag{4.1}$$

where $\bar{u}$ is the mean horizontal wind speed and z the height of the sensor. It can be used to calculate the minimum area of uniform terrain in order to get an undisturbed fetch at the measuring sensors. Since there are no detailed information about the measurement site, it is only taken into account on the avoidance of flow disruption by forests. Since the wind speed and vegetation differs with direction, it is important to estimate L_x in respect to the wind direction. The data for the wind direction and speed are taken from the lowest measurement height of the $9-\mathrm{m}$ mast. Since the two dimensional sonic anemometer is a more precise instrument, a comparison between the sonic anemometer and the wind vane and cup anemometers is made. Therefore the wind speeds and the

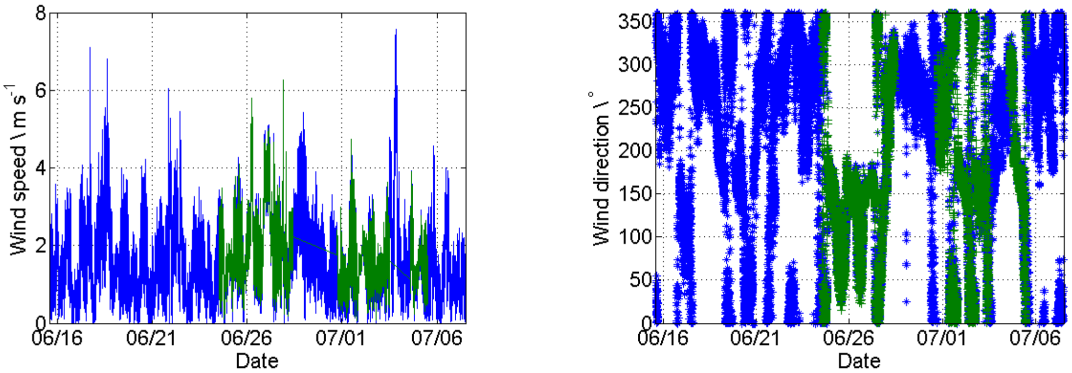

Figure 4.1: *Comparison of wind speed and wind direction measured by a two dimensional sonic anemometer (—, *), a cup anemometer (—) and a wind vane (*). No significant differences are visible.*

directions for the certain measurement instruments are plotted in the same figure against time. Figure 4.1 shows that there are no significant differences between the wind data. The classification of the different wind sectors due to their flow disturbing potential is a procedure taken from Högström (1988). The map of the measuring area (figure 3.4) shows that there is at least one wind sector with very little distance to a forest. This sector ranges from 50 to 130 ° where the distance to the trees is less than 200 m. This means that data with fetch from this direction have to be excluded when they are linked with large values of L_x. Figure 4.2b shows a histogram of the wind direction for 30 minute averaged data and additionally gives the range of different L_x. Since it is assumed that much higher ($\gg$) means a value of ten, L_x is already multiplied with ten in figure 4.2b and therefore can be directly related with the minimum distance which is necessary to get an undisturbed fetch. The mean wind direction within a 30 minute time period is calculated by transforming the angles given in degrees in a Cartesian coordinate system. All considerations are also done for 15 minute time periods. It is visible in figure 4.2b that there are no cases for the 'small distance sector' in which L_x, m is larger than the distance to the disturbing trees. Therefore no data have to be excluded due to disturbed fetch.

In the processing of the data from the BLLAST campaign, the assessment of the data on the basis of the wind direction is used in a further way. To reduce the scatter in the final calculation of the universal functions, only data are considered which was sampled under fair weather conditions. Therefore time periods in which synoptic pressure gradients are important are excluded. In order to identify these time periods, it is made use of the local wind regime. This local wind regime, described in detail in section 3.1 implies wind from north during daytime and wind from south at night. This means only data are considered which was sampled when the wind was blowing from these directions. Figure 4.2a shows the histogram of the wind direction and the range of the wind speed

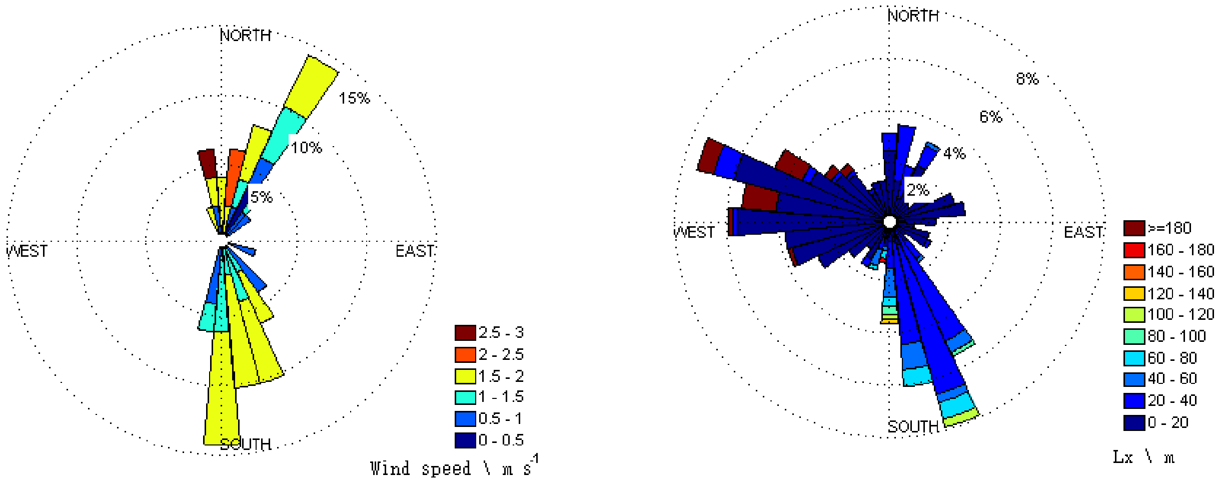

(a) (b)

Figure 4.2: *(a) Wind rose for the 1st of July noon until the next day noon. Additional information about the wind speed is given. It is visible that the main wind directions are north and south and the average wind speed is about* 2 m*. (b) Histogram of the wind speed for the whole time period. It contains additionally information about the length scale of inhomogeneity. It is visible that wind from the east has a length scale of inhomogeneity of less than* 40 m*.*

for each direction for the 1st July as an example for a day with fair weather conditions. The main wind directions north and south can be identified easily there. On the basis of this day, the southern wind sector is chosen from 140 to 200 ° and the northern one ranges from 300 to 50 °.

In order to estimate if a time period of 15 minutes and accordingly 30 minutes, can be allocated to the mesoscale wind circulation, a 'boolean method' is used. In this method, all one minute averaged data are classified into 'good' or 'bad'. This means, if the wind direction of this one minute averaged data are north during daytime or south at night, the time period gets a value of one. Otherwise it gets a value of zero and it is assumed that this time period is not consistent with the mesoscale wind system. This method is used due to the differences of the wind direction fluctuations during daytime and night. It was already mentioned in section 3.1 that the fluctuations in the wind directions are high during daytime due to buoyancy effects. For this reason, it is assumed that the wind belongs to the mesoscale system when at least two thirds of the particular averaging time period (15 or 30 minutes) has a boolean value of one. For night, the situation was different and therefore another system was used. Since the universal function is very sensitive in stable conditions (Wyngaard, 2010), the first requirement to the time periods is that all one minute averaged data within the selected averaging time period must have a boolean value of one. The second requirement is based on the observation of temporary changes in the flow direction at night in section 3.1. Time periods in which a peak in the plot of the wind direction (figure 3.2a) is visible causes high scatter. For this reason, these time intervals are not considered in the final analysis. Therefore the standard deviation of the 15 one minute averaged data of wind direction is calculated for the time periods at night and a threshold of 20 ° is set for this standard deviation.

4.2. Temperature gradients

The gradients are only calculated for the time periods in which already fair weather conditions are assumed. In order to calculate the temperature gradients, a second-order polynomial in z is fitted through the levels of averaged temperature data (Högström, 1988):

$$\overline{T} = A + B\ln(z) + C(\ln(z))^2. \tag{4.2}$$

The independent parameters A,B and C are determined by the method of least squares. Usually the potential temperature θ has to be used to exclude temperature changes due to the decrease of pressure with height. But since the BLLAST data are measured within the lowest 2 m of the atmospheric boundary layer, where pressure changes with height are negligible, the air temperature is used instead of the potential temperature (Foken, 2006).

This means the second-order polynomial has to be derived with eight levels of 15 minute and accordingly 30 minute averages of air temperature. To reduce the error in the final calculation of the dimensionless gradients, the adjusted coefficient of determination R^2_{adj} (see Appendix A.1) is used as a parameter for the goodness of the profiles. For the calculation of the gradients only fits with a value higher than 0.96 for R^2_{adj} are used. This threshold is set because it delivers the smallest error in the final calculation of the final universal function.

Figures 4.3a and 4.3b show the profiles of the half-hour averaged temperature data for stable and unstable stratification and the fitted curves. The same plot is done for logarithmic height in figures 4.3c and 4.3d. It can be seen that there are much more data available for stable conditions than for unstable conditions and that the fitted curves fit well to the data. The gradients are calculated by derivation of equation 4.2:

$$\frac{\partial\overline{T}}{\partial z} = \frac{B}{z} + \frac{2C\ln(z)}{z} \tag{4.3}$$

For the final analysis only gradients where considered which are consistent with height. This means that in stable conditions, the gradient has to be positive for all heights and in unstable conditions just the other way around. It should also be mentioned here that this procedure could lead to the elimination of neutral conditions, because for gradients close to zero sign changes caused by the model can happen easily. The gradients can be seen in figures 4.4a and 4.4b plotted against the logarithmic height. For stable stratification the range of the temperature for the lowest thermocouples is very large. There are even time periods for which the gradients get smaller for the lowest height. This behaviour of the gradients has an impact on the dimensionless gradients, too.

Finally 177 15 minute and 96 half-an-hour time intervals are left for which steady state conditions, horizontal homogeneity and fair weather conditions can be assumed and a temperature gradient is available.

4.3. Universal functions

To derive the universal functions $\Phi_{H,B}$, the dimensionless gradients have to be plotted against the dimensionless height ς. For the dimensionless height, the Obukhov length is needed. Since the Obukhov length contains a buoyancy term $(g/\overline{T}_v)$, the virtual potential temperature should be used for its calculation. Additionally, Nicholls and Smith (1982) predicted that the buoyancy heat flux $\overline{w'T_v'}$ has to be applied instead of the turbulent heat flux. Usually the sonic anemometer measures approximately the virtual temperature, but since the data were already processed, only the turbulent heat flux is available. Commonly it is assumed that the buoyancy flux is approximately $10 - 20\%$ larger than the heat flux (Foken, 2006). The error which can occur by this assumption is estimated in section 5.2. Figure 4.5 shows the diurnal evolution of L. It can be seen that all data points have the predicted sign compared to the theoretical values in figure 2.2.

The dimensionless gradients are calculated with a von Kármán constant $\kappa = 0.4$. In order to compare the final universal function with the universal functions found in literature and modified by Högström (1988), the value for $\Phi_H(0)$ has to be the Prandtl number, set as $\mathrm{Pr}_t = 0.95$ (see equation (2.31)).

4.4. Roughness length

The roughness length z_0 is defined as the height in which the mean wind speed becomes zero. It is also called aerodynamic roughness length, because its true value can only be calculated from measurements of wind speed (Stull, 1988). For the calculation of the roughness length, an extrapolation of the logarithmic wind profile in a neutral stratification is necessary. For this reason a linear regression is used which can be derived from the logarithmic wind profile:

$$\ln(z)(u) = A + B \cdot u. \tag{4.4}$$

That means for $u = 0$ equation (4.4) yields $\ln(z(0)) = A$. The theoretical method can be seen in figure 4.6. For this reason wind profiles are calculated over a time period of 15 minutes every quarter hour. Also a calculation with 30 minute averaged time periods took place. The following assumptions are used to guarantee that neutral conditions are predominant and the calculated value of z_0 is realistic:

1. neutral conditions are assumed, when the difference between the temperature of two levels is less than 0.3 K

2. $z_0 = \exp(A)$ has to be bigger than zero
3. R^2 (see Appendix A.1) has to be larger than 0.998

This leads to 96 profiles which can be used for the final calculation of the roughness length. Figure 4.7 shows the mean wind speed for neutral conditions against logarithmic height. A mean roughness length of $z_0 = 1.59 \pm 0.89\,\mathrm{cm}$ is found. For 30 minute averaged time periods,42 wind profiles are found and a mean roughness length of $z_0 = 1.48 \pm 0.73\,\mathrm{cm}$ is estimated. For the further considerations, the 15 minute averaged data are used, because of the larger number of profiles.
Compared to tabulated values for grass plains, the calculated value of 1.59 cm fits well. For example Etling (2008) set a range of 0.1 to 4 cm and Foken (2006) 0.005 to 0.2 m for the roughness length over a surface covered by grass. The roughness length is useful to identify the minimum height in which M-O similarity is applied by theory (see section 2.6.3).

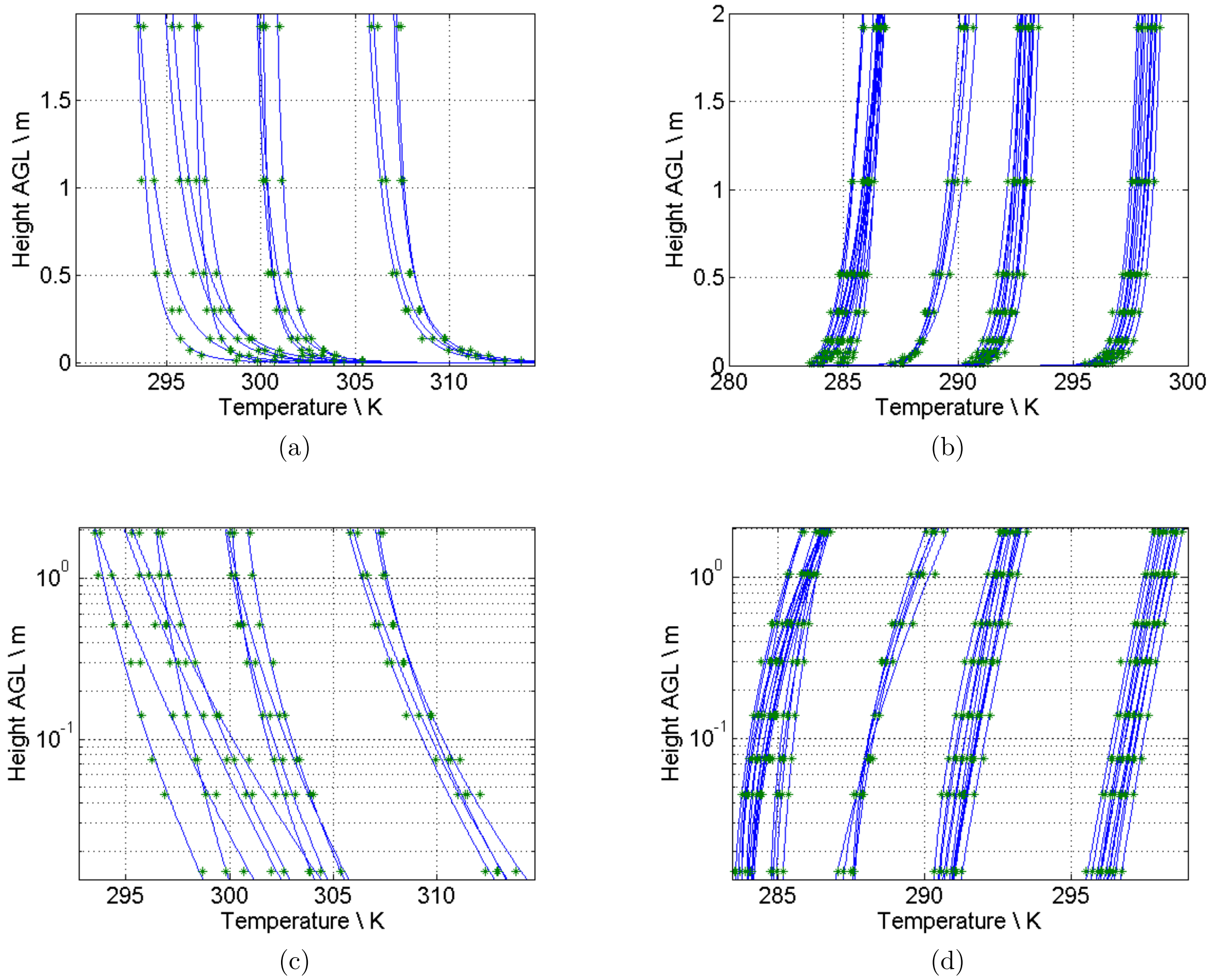

Figure 4.3: *Profiles of the mean air temperature and fitted second-order polynomial for unstable (left) and stable (right) stratification for half an hour averaged temperature data ((a) and (b)). It can be seen that the fitted curves fit well to the measured data. Profiles of the mean air temperature and fitted second-order polynomial against logarithmic height ((c) and (d)).*

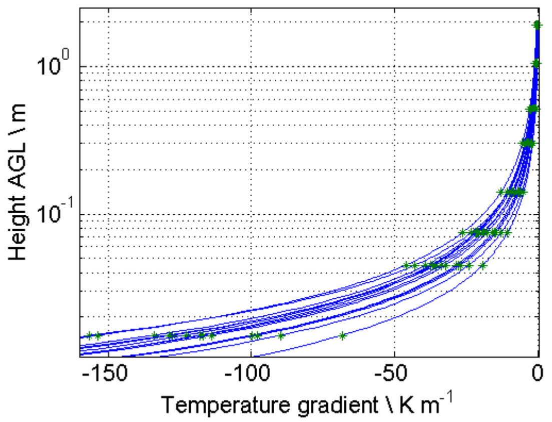

(a)

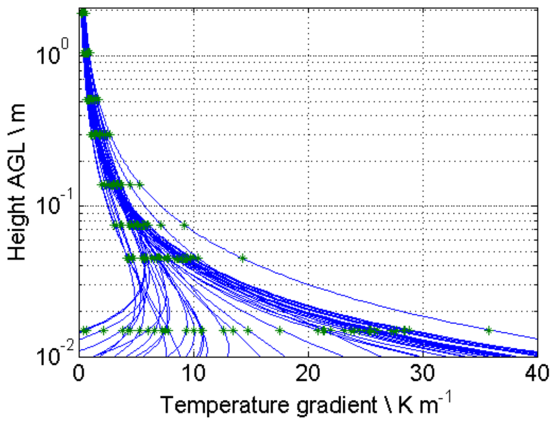

(b)

Figure 4.4: *Temperature gradients against the logarithmic height ((a) and (b)). For stable stratification (right) it can be seen that the gradient of the lowest thermocouples has a wide range and does not necessarily has the largest gradient. This behaviour of the gradient for the lowest height does affect the dimensionless gradients which will be seen in section 5.4.*

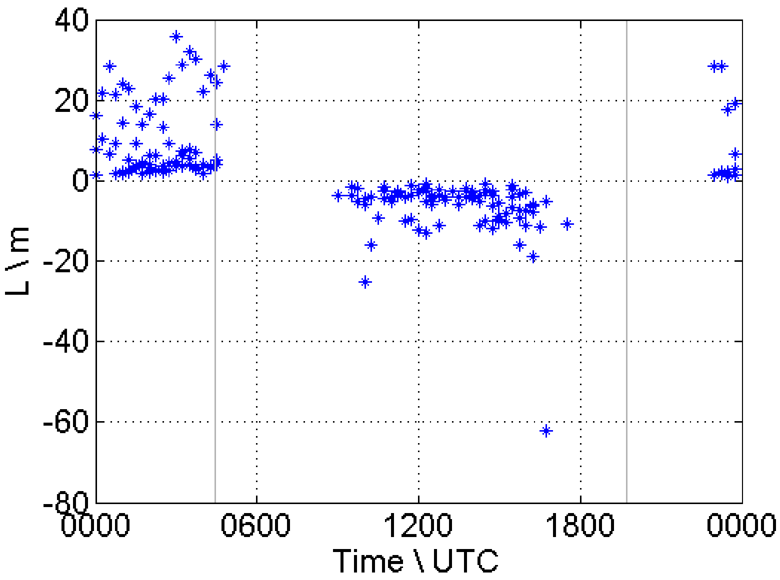

Figure 4.5: *Diurnal evolution of the Obukhov length. It can be seen that the sign and the values fit to the expected theoretical ones which can be seen in figure 2.2. The vertical grey line indicate sunrise and sunset.*

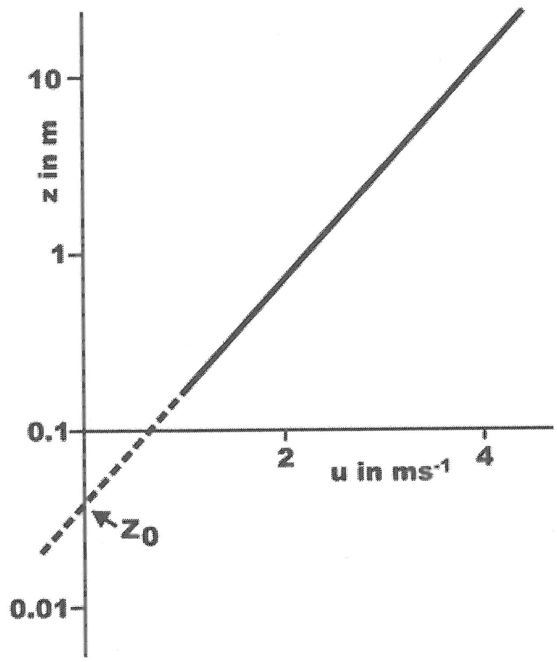

Figure 4.6: *Theoretical experimental determination of the aerodynamic roughness length. The mean wind speed is plotted versus logarithmic height and extrapolated towards the y-axis. The intersection with the y-axis gives the logarithmic value of the roughness length (Foken, 2006).*

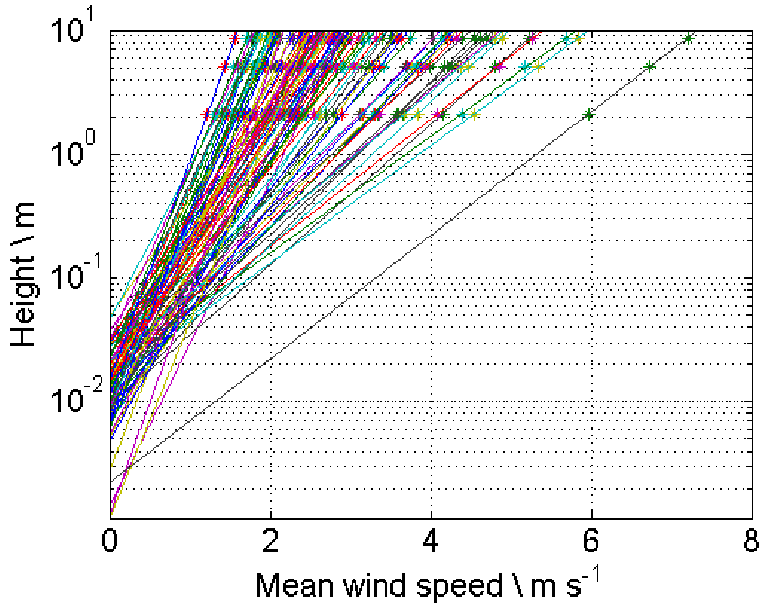

Figure 4.7: *Wind profiles for neutral conditions against logarithmic height. The profiles are calculated for 15 minute averaging time period. The mean roughness length* $z_0 = 1.59 \pm 0.89\,\mathrm{cm}$.

5. Results and Discussion

5.1. Comparison to theory

In section 2.6.3 it was already mentioned that the most advised formulations for the universal functions are the ones of the KANSAS experiment, modified by Högström (1988): $\Phi_{H,K}$ (see table 2.1). In the following, it is assumed that these functions are true and the data will be assessed relatively to this formula. In addition $\kappa = 0.4$ and $\mathrm{Pr}_t = 0.95$ are considered as true constants. In a first step the dimensionless gradients are calculated for every height and for both, 15 and 30 minute averages. Figure 5.1 shows the plots of the dimensionless gradients against ς for all measurement heights by thermocouples and both averaging periods, respectively. The plots also contain the fitted functions $\Phi_{H,B}$, following equations (2.31) and $\Phi_{H,K}$. The formulations of $\Phi_{H,B}$ are given in tables A.1 and A.2 in the Appendix. The comparison of $\Phi_{H,B}$ and $\Phi_{H,K}$ for each height shows that there are significant changes with respect to height. These changes differ for both stability cases. It can also be seen that the differences between $\Phi_{H,B}$ and $\Phi_{H,K}$ have the tendency to become smaller with height. The range of ς gets larger with increasing height. The reason for this is mainly the implementation of the measurement height in the formulation of the dimensionless height $\varsigma = z/L$.
In section 2.6.3 it was already mentioned that a vertical limitation for the M-O similarity theory exists for z/z_0 much higher than one. For this reason the ratios between the measurement heights and the roughness length are calculated and listed in table 5.1. For z_0, the found value of 1.59 cm (see section 4.4) is used. If it is assumed that 'much higher' means a factor of greater than ten, the M-O similarity will only be applied for thermocouples #5 to #8. Therefore all data points for the upper four thermocouples are taken and plotted against ς then, common $\Phi_{H,B}$ function for all heights is fitted. This is done again for 15 and 30 minute averaging time, respectively. The formulations for $\Phi_{H,B}$ are listed in table 5.2. The uncertainty of the fitted functions is given by the root mean squared error (see Appendix A.1). Figure 5.2 shows the plots of the dimensionless gradients, $\Phi_{H,B}$ and $\Phi_{H,K}$. The comparison of the two averaging time periods differs for stable and unstable conditions. For stable stratification, there is no significant difference

#	1	2	3	4	5	6	7	8
z/z_0	0.943	2.83	4.72	8.81	18.9	32.4	65.7	121

Table 5.1: *Ratio between the sensor height to the roughness length.*

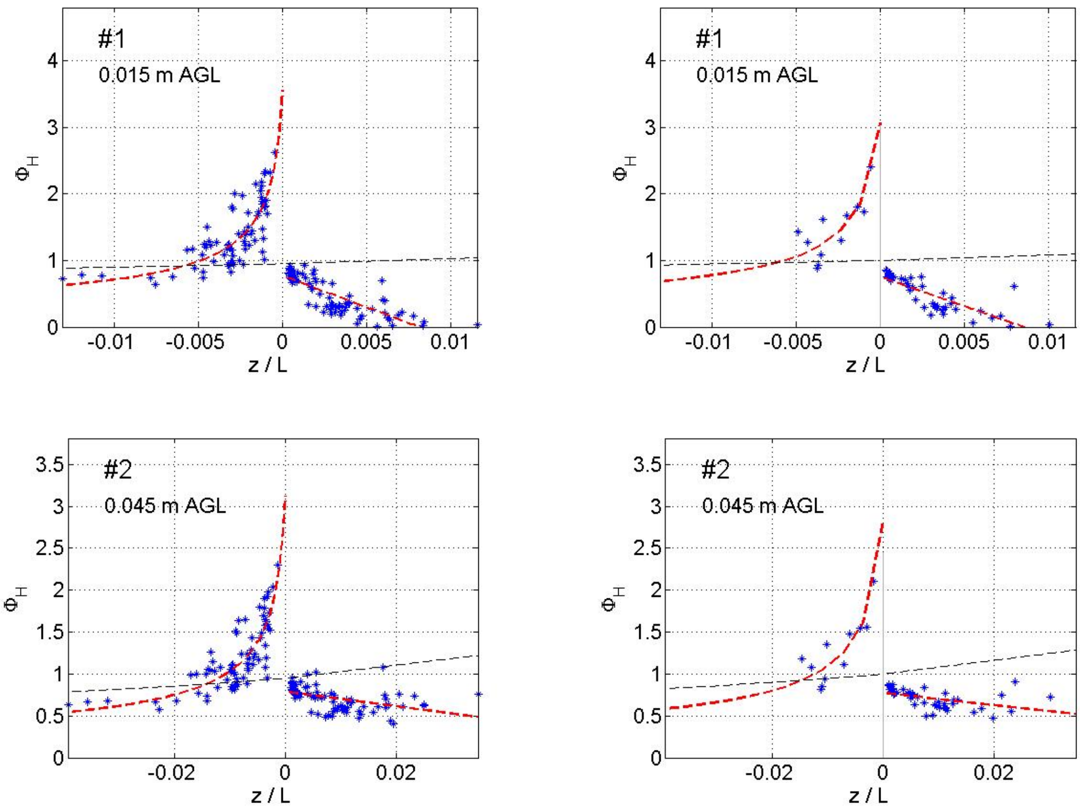

Figure 5.1: *The dimensionless gradients for temperature (*) for every thermocouple level are plotted against dimensionless height ς. On the left side the 15 minute averages data are visible and on the right side the 30 minute averaged data. Also the fitted universal functions for stable and unstable stratification $\Phi_{H,B}$ are included (—), see table A.1 and A.2) and the universal function of the KANSAS experiment $\Phi_{H,K}$ ((−−), see table 2.1).*

between the two formulations of $\Phi_{H,B}$. This is affirmed by the 95 % confidence intervals that are listed in the Appendix in table A.3. It can be seen that the value for Pr_t and the slope γ_2 for both averaging time periods are included in the 95 % confidence intervals of the other averaging time period. Therefore it is assumed that for stable stratification a 15 minute averaging time period can be used without causing large errors.
For unstable conditions, the values of Pr_t and γ_1 are not part of the other averaging time period. In section 4.1 it was stated that the averaging time period has to be long enough in order to include all eddy sizes. Since in a convective boundary layer large eddies are possible, it could be that a time period of 15 minutes is too short to include all eddy sizes. Furthermore it can be seen in figure 5.2a that the fit of $\Phi_{H,B}$ for 15 minute averaging time period takes smaller values of the dimensionless gradient than the experimental data points for $\varsigma < -0.5$. Since there is the requirement that $\Phi_H(0) = \mathrm{Pr}_t$, the fit for unstable stratification is forced to a value of 0.95 for neutral conditions. Table 5.3 gives the formulations of the new fitted universal functions for both averaging time periods.

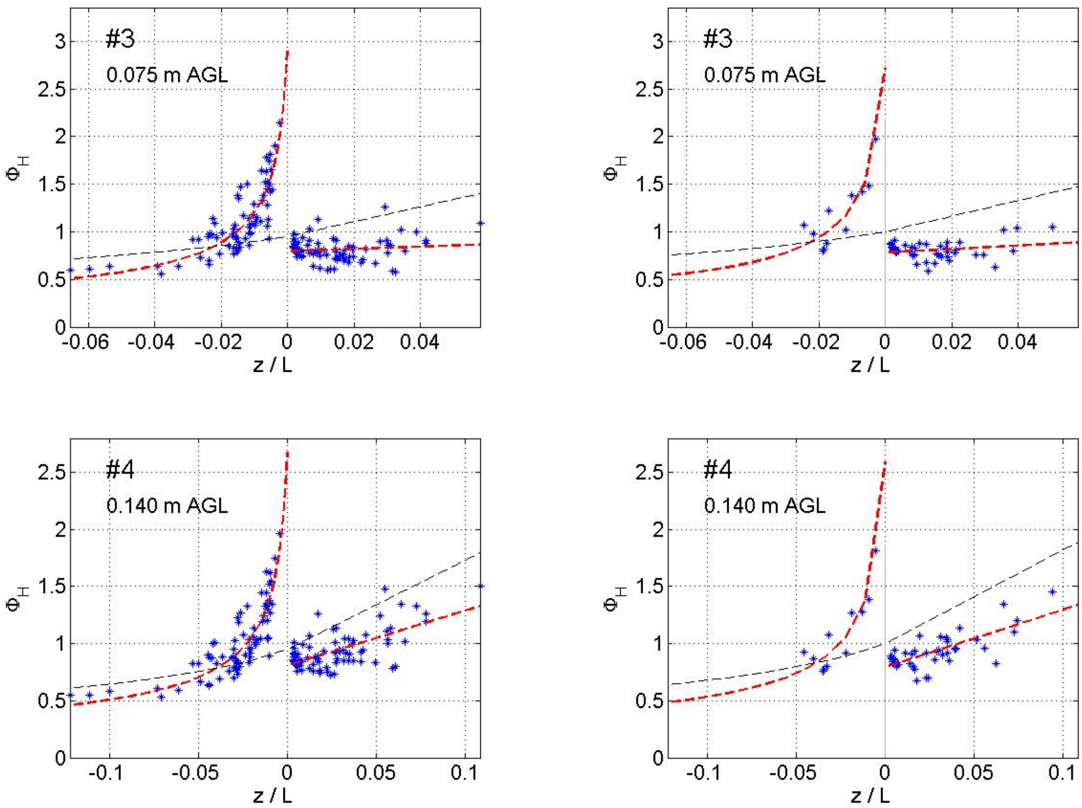

Figure 5.1: *continued*

Now, the γ_1 values are included in the 95 % confidence interval of the other averaging time period and vice versa. Figures 5.3 shows the dimensionless gradients for unstable stratification for both averaging time periods, the universal function without and with a fixed boundary and the theoretical universal function. It can be seen that for 15 minute averaging time period, the data points of the dimensionless gradients lie on the fitted universal function with a fixed boundary. In contrast they do not for 30 minutes averaging time period. Furthermore the uncertainty of the fit increases of about 3 and 7 %, respectively.

In the following, the focus will be set on the consideration of stable conditions. For this reason, in figure 5.4a only dimensionless gradients for stable stratification are plotted. Again the plot also contains the fitted universal function $\Phi_{H,B}$ and the one of the KANSAS experiment $\Phi_{H,K}$. The value of the turbulent Prandtl number for the BLLAST data is 0.955 ± 0.34 and therefore agrees well with the theoretical value of 0.95. The slope γ_2 of the linear function on the other hand is much smaller than the theoretical one. This can be seen in the formulations of the universal functions and in figure 5.4a. In fact, the slope of $\Phi_{H,B}$ is just 22 % of the theoretical one. The comparison of $\Phi_{H,B}$ for stable stratification to various functions from literature in figure 5.4b shows that γ_2

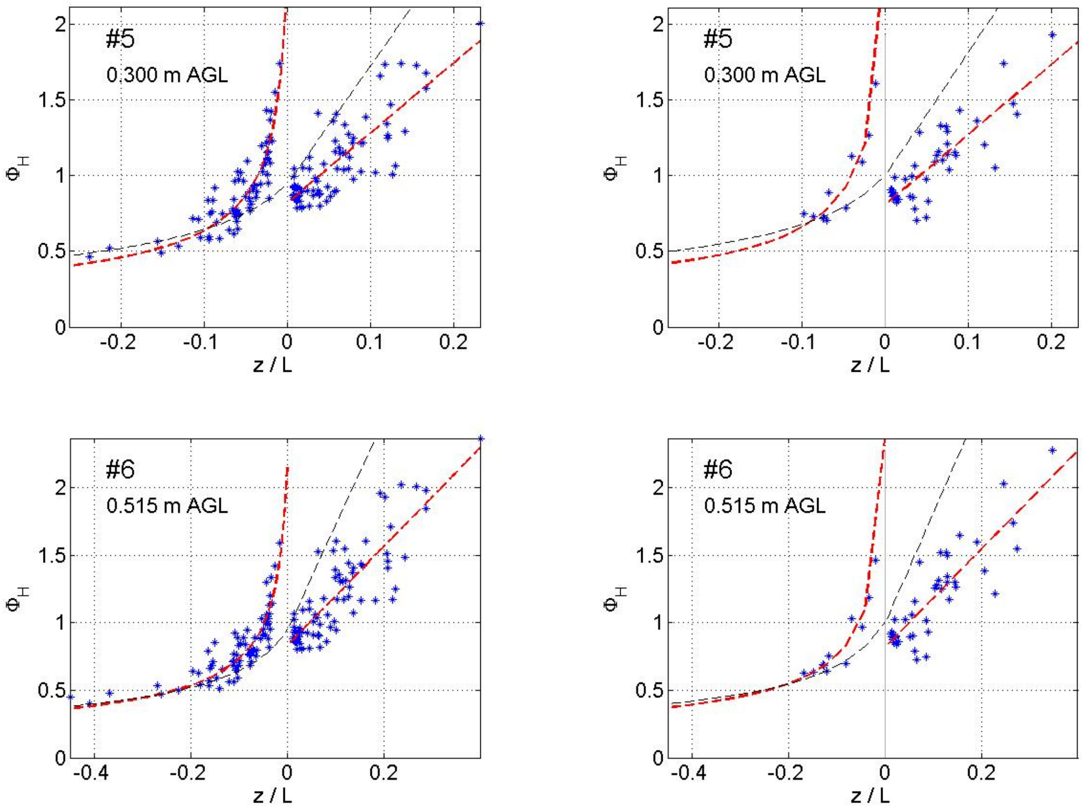

Figure 5.1: *continued*

is clearly smaller than all the other slopes, although values of γ_1 of 5.4 and 6 had been found, too. This means there is no published universal function which shows a similar behaviour for Φ_H in stable stratification.

Since these deviations of the universal function from BLLAST campaign to the theoretical value are existing, it is necessary to correct them before lower measurement heights can be analysed. Therefore the error source has to be found and an adequate correction method has to be implemented. For the calculation of the dimensionless heights different measurement variables and assumptions are necessary. This leads to several potential sources of error. These sources of error have to be found and estimated in order to find a correction method for the dimensionless gradients.

5.2. Sources of error

The measurement variables which are used for the calculation of the dimensionless gradients against ς are the temperature measurements in different heights and the turbulent fluxes of momentum and heat. Additionally, horizontal homogeneity and steady state conditions are assumed. Furthermore, the air temperature is used instead of the po-

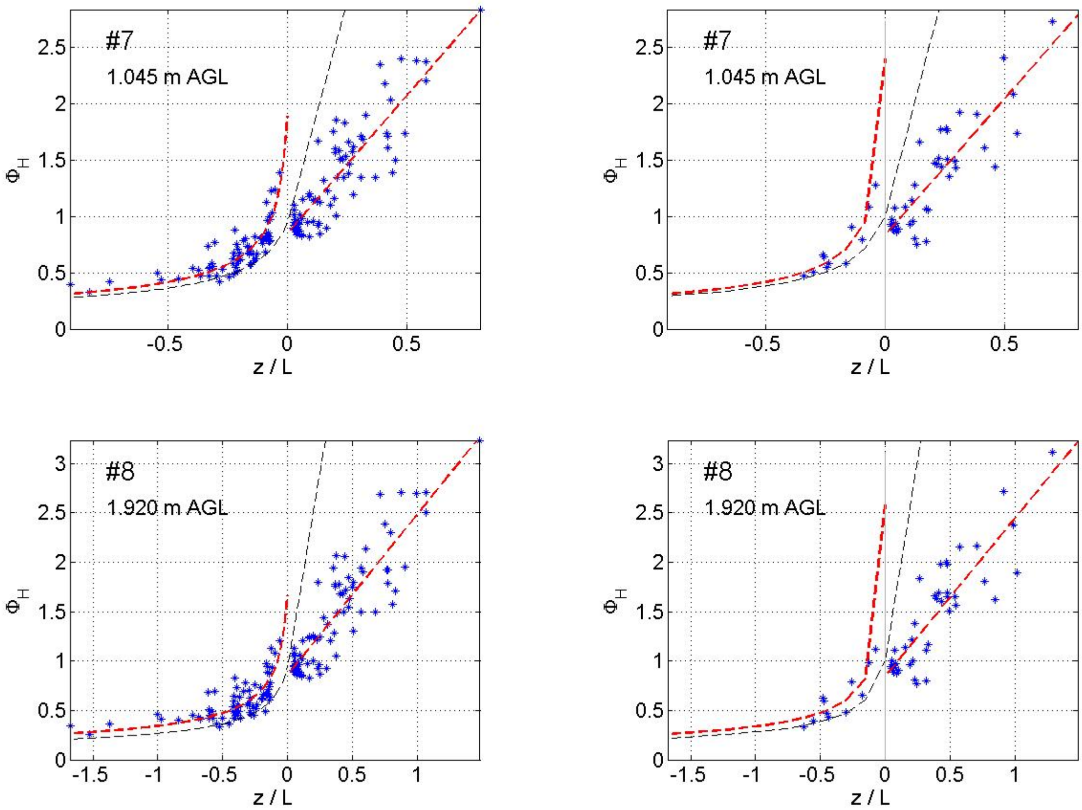

Figure 5.1: *continued*

tential and the virtual potential temperature. In a first step, these assumptions will be analysed.

In section 5.1 the steady state conditions are already assessed. It was found that there is no significant difference between the two averaging time periods for stable stratification. Incomplete horizontal homogeneity is also excluded as origin of the large differences between the dimensionless gradients (see section 4.1). Nevertheless for this assumption it should be kept in mind that the small heterogeneity is not considered and its influence not assessed. In section 4.2 it was predicted that the use of the air temperature instead of the potential temperature does not cause remarkable errors. It was already mentioned in section 4.3 that for the calculation of the Obukhov length, the virtual temperature and the buoyancy flux should be used instead of the air temperature and the turbulent heat flux, (Högström, 1988). In order to assess the influence of this assumption, the Obukhov length in its true definition is calculated for several time periods in which the necessary data were available. The calculation of the buoyancy flux was done with the expression (Wyngaard, 2010):

$$\overline{w'T_v'} \approxeq \overline{w'T'} + 0.61\overline{T}\overline{w'q'} \tag{5.1}$$

where $\overline{w'q'}$ is the turbulent latent heat flux. Comparison to the used dimensionless gradients show that there is a difference of 2 % at the most. This is small compared to the

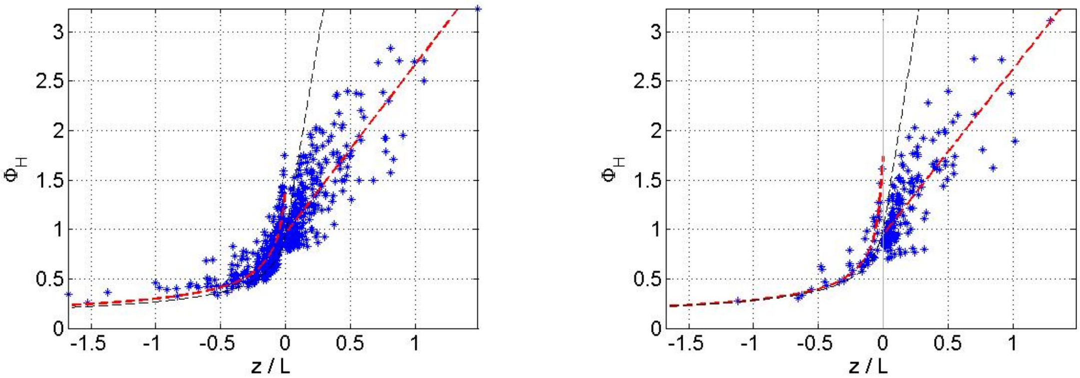

(a) (b)

Figure 5.2: *The dimensionless gradients (*) are plotted versus ς. This is done for the upper four thermocouples and for averaging periods of 15 minutes (a) and 30 minutes (b). Additionally the fitted universal function (−−) and $\Phi_{H,K}$ (−−) are plotted.*

Averaging Period	Formulation	*RMSD* %	stratification
15 min	$1.40 \cdot (1 - 20.9\varsigma)^{-1/2}$	13.8	$\varsigma < 0$
30 min	$1.74 \cdot (1 - 36.9\varsigma)^{-1/2}$	12.5	$\varsigma < 0$
15 min	$0.955 \cdot (1 + 1.79\varsigma)$	24.8	$\varsigma \geq 0$
30 min	$0.947 \cdot (1 + 1.76\varsigma)$	25.3	$\varsigma \geq 0$

Table 5.2: *Formulations for the universal function with data from BLLAST campaign. The fourth upper thermocouples are used for the fit. The 95 % confidence intervals can be found in the Appendix in table A.3*

whole uncertainty of the universal function in stable stratification of 24.8 %. Therefore it can be assumed that no significant error occurs by using $\overline{T}$ instead of $\overline{T}_v$ and $\overline{w'T'}$ instead of $\overline{w'T'_v}$. With these considerations it is supposed that non of the assumptions is responsible for the deviation of the dimensionless gradients of BLLAST data to the universal function of the KANSAS experiment.
For this reason, the measured variables have to be considered. The temperature measurement of the thermocouples was already discussed in detail in section 3.2.1. A systematic error was found which was already corrected. This means, the air temperature can be ruled out as the measurement variable which is responsible for the error in the dimensionless gradients.
As a result, the fluxes are left as possible source of error. In addition to the above made exclusion procedure, there is another reason for doubting the measurement of the eddy covariance station. Eddy covariance measurements are more complex than direct measurements of temperature. Högström (1988) already predicted that errors due to flow distortion (see section 2.6.3) causes deviations of the various universal functions. The complexity of eddy covariance measurements is further illustrated in Lee et al. (2004).

Averaging Period	Formulation	$RMSD$ %	stratification
15 min	$0.950 \cdot (1 - 5.04\varsigma)^{-1/2}$ (5.75, 4.33)	17.0	$\varsigma < 0$
30 min	$0.950 \cdot (1 - 4.92\varsigma)^{-1/2}$ (6.97, 2.88)	19.9	$\varsigma < 0$

Table 5.3: *Fitted universal functions for unstable stratification. Pr_t is forced to a value of 0.95. For γ_1, the 95 % confidence intervals are listed in brackets. The uncertainty is given as the root mean squared error.*

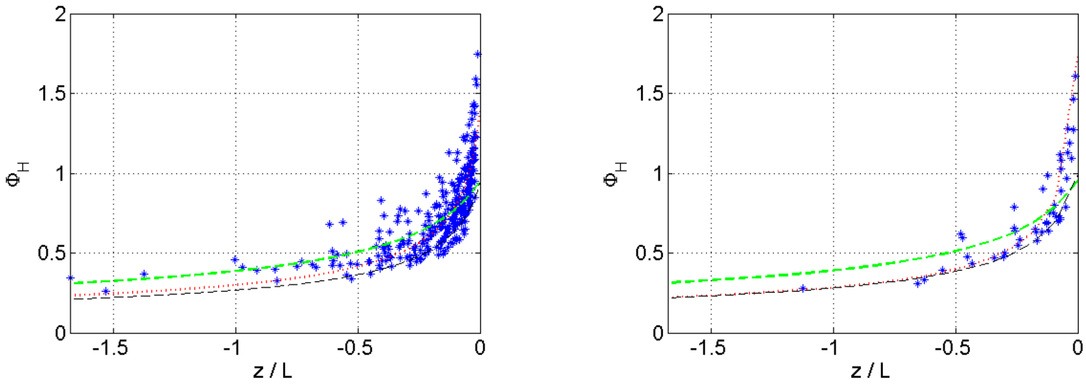

(a) (b)

Figure 5.3: *Dimensionless gradients for unstable stratification (*), universal function with fixed boundary (−−), without fixed boundary (...) and the theoretical universal function (−−) for 15 minutes (a) and 30 minutes (b) averaging time period.*

The flux dependent variables of the dimensionless gradients are the turbulent heat flux and the friction velocity. This means that both are affected when a systematic measurement error exists. Since there is no eddy covariance station in the close-by environment, there is no possibility to assess the fluxes by comparison. In a first step, the fluxes are assessed qualitatively. This already happens in section 4.3 by showing that the Obukhov length is following its diurnal cycle. Another parameter which is considered is the behaviour of scaling temperature ϑ_* against the gradients for the upper four thermocouples. The temperature gradient is taken as an indicator for the stratification. In unstable conditions, the temperature decreases with height and therefore the temperature gradient $\partial \bar{T}/\partial z$ is negative. In stable conditions, it is the other way around. Figure 5.5 shows the plot for this consideration. Since the same value of the fluxes is taken for every height, ϑ_* does not change with height. The variable which differs for the specific heights is the gradient. It can be seen in the plot that the gradient becomes smaller with height. This is consistent with the plots of the gradients against the logarithmic height in figure 4.4. From the behaviour of the scaling temperature in unstable conditions it

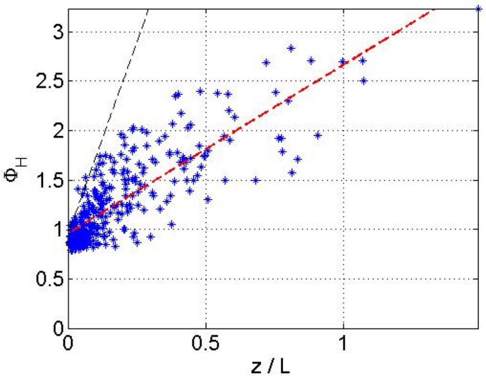

(a)

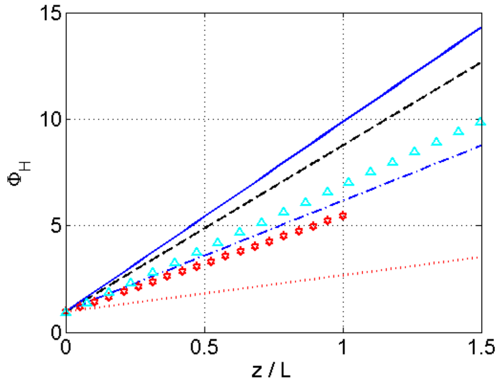

(b)

Figure 5.4: *The dimensionless gradients (*) for the upper four thermocouples are plotted against ς and the universal functions (...) are fitted through the data (a). The plot also includes the universal function of KANSAS experiment (−−). (b) $\Phi_{H,B}$ in comparison with various formulations of Φ_H. The plot contain the functions predicted by Tschalikov (1968) (-.),Dyer (1974) (⋆),Gavrilov and Petrov (1981) (△) and Zilitinkevich and Tschalikov (1968) (—). These universal functions are taken from Foken (2006). The formulations of the various universal functions can be found in table A.4*

is visible that ϑ_* becomes larger with decreasing gradients. In very unstable conditions, the turbulent heat flux takes large positive values due to buoyancy effects which are not balanced by the friction velocity. For stable conditions, ϑ_* seems to stay constant along the temperature gradient. This means the negative turbulent heat flux is balanced by the friction velocity.

5.3. Correction of the fluxes for stable stratification

The aim of the correction of the flux dependent variables is to reach their theoretical value. These theoretical values are defined as the values which the fluxes must have so that the fit through the corrected dimensionless gradients equals $\Phi_{H,K}$. In the following, the measured flux-dependent variables are expressed with a tilde: $\tilde{\overline{wT'}}$, $\tilde{u}_*$, $\tilde{L}$ and $\tilde{\vartheta}_*$, to distinguish them from the theoretical values. Additionally, $\Phi_{H,K}$ will be expressed as Φ_H and $\Phi_{H,B}$ as $\tilde{\Phi}_H$.

It is assumed that constant 'correction factors' a and b exist. This means that the systematic error of the eddy covariance station is supposed to be independent of other atmospheric parameters. The theoretical values of the flux dependent variables can be derived by their measured values and the 'correction factors':

$$\overline{w'T'} = a \cdot \tilde{\overline{w'T'}} \tag{5.2}$$

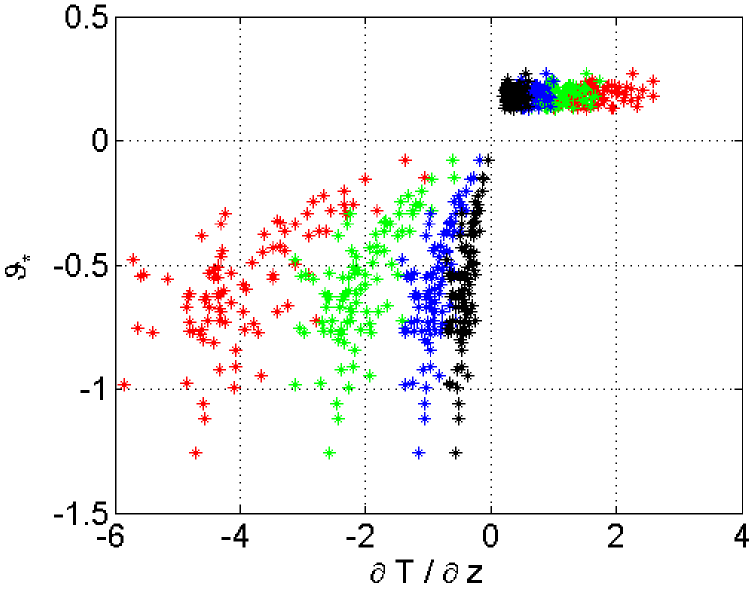

Figure 5.5: *Scaling temperature versus the calculated temperature gradient for thermocouple #5 (*), #6 (*), #7 (*) and #8 (*). Since ϑ_* is the same for all heights, only the gradients in the figure differ for the certain heights.*

$$u_* = b \cdot \tilde{u}_* \tag{5.3}$$

For the scaling temperature it follows:

$$\vartheta_* = c \cdot \tilde{\vartheta}_* \tag{5.4}$$

where $c = a/b$. In a first conceptual consideration, it is assumed that $\tilde{\overline{wT'}}$, $\tilde{u}_*$ or $\tilde{\vartheta}_*$ is already consistent with its theoretical value. These considerations are only made graphically and no 'correction factors' are calculated.

5.3.1. Conceptual consideration

In the first conceptual consideration the measured turbulent heat flux is taken as consistent with its theoretical value ($a = 1$). Figure 5.6 shows a sketch for the theoretical universal functions Φ_H and $\tilde{\Phi}_H$. In the figure also a data point for dimensionless gradient is plotted which lies on $\tilde{\Phi}_H$. Since the dimensionless gradient is inverse proportional to the scaling temperature and the turbulent heat flux is taken as consistent with its theoretical value, only a change in the friction velocity can influence the value for the dimensionless gradient. The dimensionless gradients and u_* are proportional to each other. On the other hand the dimensionless height is inverse proportional to the friction velocity to the power of three. It is shown in the figure 5.6 how a change of u_* affects

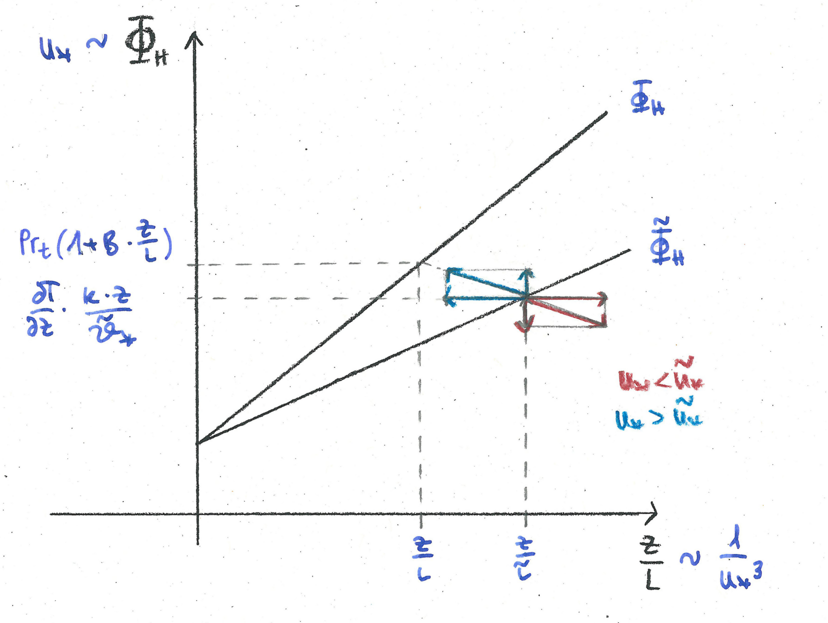

Figure 5.6: *Conceptual consideration for the behaviour of $\tilde{\Phi}_H$ for $\overline{w'T'} = \widetilde{\overline{w'T'}}$. Is is visible that the correction factor of $\tilde{u}_*$ has to be larger than one.*

the data point. In case that the measured friction velocity is overestimated compared to its real value it would not be possible for the data point to reach Φ_H. Only if $\tilde{u}_*$ is underestimated, the theoretical universal function can be reached. This means that b must have a value larger than one.

In a next step, the conceptual consideration is done with the friction velocity taken as consistent with its theoretical value ($b = 1$). Figure 5.7 shows a similar sketch as in figure 5.6. It can be seen that $\overline{w'T'}$ is inverse proportional to the dimensionless gradient and directly proportional to the dimensionless heigh. Therefore, the 'correction value' a has to be smaller than one so that the corrected dimensionless gradient is able to reach Φ_H.

In the last conceptual consideration, it is assumed that the scaling temperature matches its theoretical value ($c = 1$). This means the ratio of $\widetilde{\overline{w'T'}}$ and $\tilde{u}_*$ is taken as consistent with their theoretical ratio ($a = b$). Again the consideration is done graphically in figure 5.8. Beside Φ_H and $\tilde{\Phi}_H$, two data points are plotted into the figure. The first one is settled on $\tilde{\Phi}_H$ and the second one is plotted near the neutral range below the value of $\Phi_H(0)$. Since the dimensionless gradients are proportional to ϑ_*, there is no change for the y-axis when $\widetilde{\overline{w'T'}}$ and $\tilde{u}_*$ are corrected with the same factor. However, the x-axis is inverse proportional to the squared friction velocity. This means in case of a 'correction factor' of $b > 1$, the data points will be shrinked along the x-axis and in case of $0 < b < 1$, the points are stretched along the x-axis. Therefore b has to be higher than

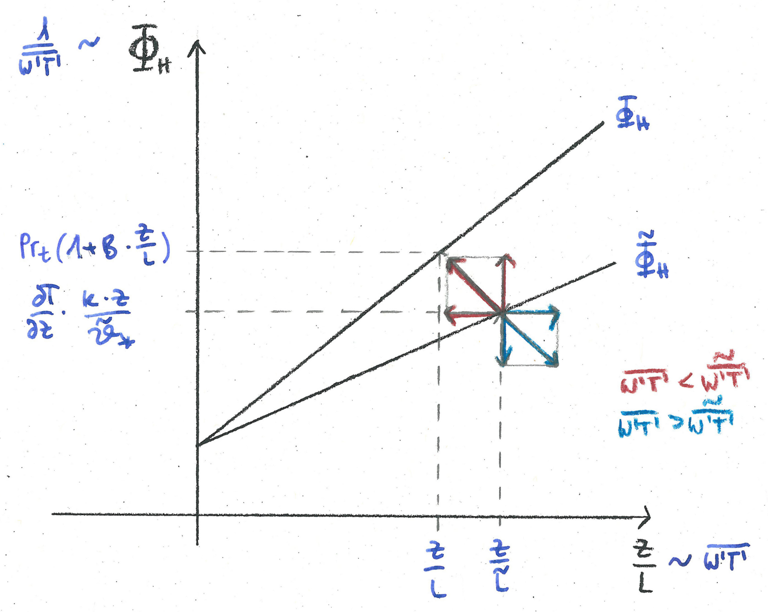

Figure 5.7: *Conceptual consideration for the behaviour of $\tilde{\Phi}_H$ for $u_* = \tilde{u}_*$. It is visible that for this approach only a correction factor $a < 1$ is possible.*

one so that the dimensionless gradients can reach their theoretical value. Considering the data points for near neutral conditions, it is visible that for all values which lie below $\Phi_H(0)$, it is not possible to reach the theoretical universal function.

5.3.2. Correction factors

In order to find the values for a and b, the following it is started with the following equation:

$$\frac{\partial \overline{T}}{\partial z}\frac{\kappa z}{\vartheta_*} = \mathrm{Pr}_t \cdot (1 + B\frac{z}{L}), \tag{5.5}$$

where B is the slope of the theoretical universal function for the stable case ($\varsigma > 0$) and therefore has a value of 8.2 (see table 2.1). The requirement of equation (5.5) is that the dimensionless gradient calculated with the theoretical values of the flux dependent parameters has to be the same as the theoretical universal function. By inserting expressions (5.3) and (5.4) into equation (5.5), the following expression can be achieved:

$$\frac{\partial \bar{T}}{\partial z}\frac{\kappa z}{\tilde{\vartheta}_*}\frac{1}{c} = \mathrm{Pr}_t + B \cdot \mathrm{Pr}_t \cdot \frac{z\kappa\tilde{\vartheta}_*}{\bar{T}\tilde{u}_*}\frac{c}{b^2}. \tag{5.6}$$

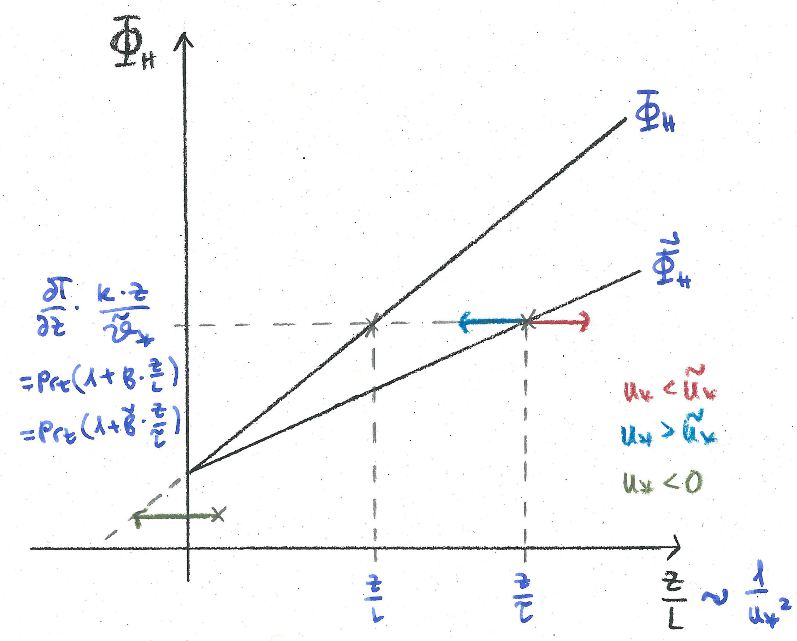

Figure 5.8: *Conceptual consideration for the behaviour of $\tilde{\Phi}_H$ for $\vartheta_* = \tilde{\vartheta}_*$. Is is visible that for such an approach only the range of ς changes.*

This equation can be simplified by inserting $\tilde{L}$ and $\tilde{\Phi}_H$, whereupon $\tilde{\Phi}_H$ represents the calculated dimensionless gradients:

$$\tilde{\Phi}_H = \mathrm{Pr}_t \cdot c + B \cdot \mathrm{Pr}_t \frac{z}{\tilde{L}} \frac{c^2}{b^2}. \tag{5.7}$$

This formulation is used to arrange a linear system of equations. Therefore a new variable $u \equiv c^2/b^2$ is introduced. The linear system of equations has the following form:

$$\begin{pmatrix} \tilde{\Phi}_{H,1} \\ \tilde{\Phi}_{H,2} \\ \cdots \\ \tilde{\Phi}_{H,i} \end{pmatrix} = \begin{pmatrix} \mathrm{Pr}_t & B \cdot \mathrm{Pr}_t \cdot \frac{z}{\tilde{L}_1} \\ \mathrm{Pr}_t & B \cdot \mathrm{Pr}_t \cdot \frac{z}{\tilde{L}_2} \\ \vdots & \vdots \\ \mathrm{Pr}_t & B \cdot \mathrm{Pr}_t \cdot \frac{z}{\tilde{L}_i} \end{pmatrix} \cdot \begin{pmatrix} c \\ u \end{pmatrix},$$

where $\tilde{\Phi}_{H,1}, \tilde{\Phi}_{H,2}, ...\tilde{\Phi}_{H,i}$ represent all data points of the dimensionless gradients and $\tilde{L}_1, \tilde{L}_2, ...\tilde{L}_i$ their Obukhov lengths. This linear system of equations is solved for every data point and delivers the averaged correction factors $c = 1.05$, $b = 2.15$ and $a = 2.16$. The corrected dimensionless gradients are plotted in figure 5.9 and the corresponding universal functions are listed in table 5.4. For both stratification cases it can be seen that the correction of the universal function with the found values of a and b work

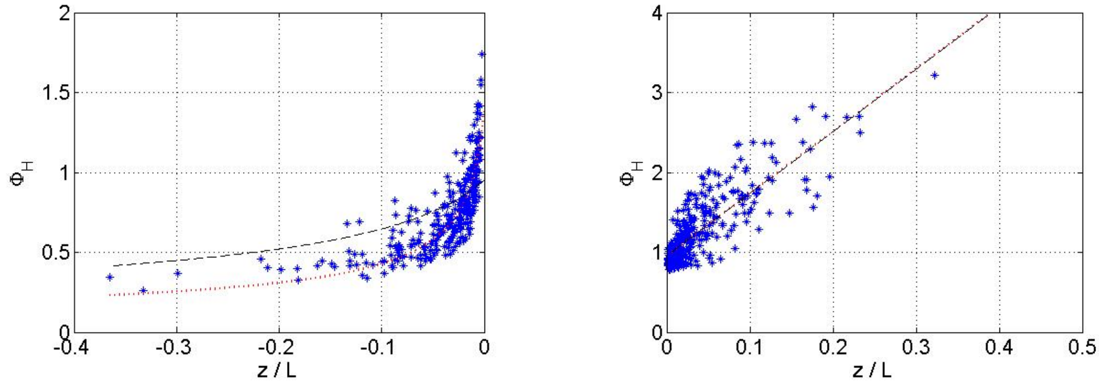

Figure 5.9: *Corrected dimensionless gradients (*) for $b = 2.15$ and $a = 2.16$. The fitted universal function (...) fit perfectly to the theoretical one (−−) for stable stratification. For unstable stratification no improvement is made.*

Formulation	$RMSD$ %	Stratification
$1.4 \cdot (1 - 25.6\varsigma)^{-1/2}$	13.8	$\varsigma < 0$
$0.950 + 7.82\varsigma$	24.7	$\varsigma > 0$

Table 5.4: *Corrected universal functions for variable fluxes. For stable stratification $\Phi_{H,K} = \Phi_{H,B}$ is reached. For unstable stratification no improvement is visible.*

well for stable conditions. The fitted universal function equals the theoretical one. For unstable conditions, no improvement is visible.
Since the 'correction factor' for the scaling temperature is approximately one, it can be assumed that ϑ_* is measured correctly. Following the third conceptual consideration (section 5.3.1), this means that in order to reach Φ_H, mainly a shrinking of the data points along the x-axis took place. A consequence of this are very small values of ς.
With c taken as one, it is also possible to reach a and b analytically. Therefore both universal functions are put into one equation. The validity of this equation is shown in figure 5.8:

$$\tilde{\mathrm{Pr}}_t \cdot (1 + \tilde{B}\frac{z}{\tilde{L}}) = \mathrm{Pr}_t \cdot (1 + B\frac{z}{L}) \tag{5.8}$$

where $\tilde{B}$ is the slope of the universal function from BLLAST campaign and has a value of 1.79 (see table 5.2). With the assumption that $\tilde{\mathrm{Pr}}_t \approx \mathrm{Pr}_t$, the expression

$$b = \sqrt{\frac{B}{\tilde{B}}} \tag{5.9}$$

can be derived. This leads to a 'correction factor' of 2.14 for a and b. This result is very similar to the 'correction factors' predicted above.

5.4. Lower thermocouples

In figure 5.1 also the dimensionless gradients for the lowest thermocouples for which the M-O similarity theory does not apply are plotted. It can be seen in the plots for the measurement heights of #1 to #3 that most of the data points for stable stratification lie below the turbulent Prandtl number ($\Phi_H(0)$). This means the correction method implemented above is not usable for these heights. This agrees with the vertical limitation for the M-O similarity theory (see section 2.6.3). For the measurement height of thermocouples #4 the situation is not that clear. There approximately one half of the dimensionless gradients lie below a value of 0.95, the other above. Since the ratio of the measurement height to the roughness length has a value of 8.81, it can already be interpreted as 'much higher' than z_0 and therefore seen as a transition case.
In order to find an explanation why the dimensionless gradients of the M-O similarity theory does not work for the lowest thermocouples, equation 2.25 is considered. It can be seen that in this formulation only the temperature gradient and z changes for the certain measurement heights. Since for thermocouples #1 to #3 most of the data points lie below the theoretical value, their dimensionless gradients are underestimated. To have similarity, $\partial\overline{T}/\partial z$ and z have to balance each other. For the lowest heights this means that the gradient is too small to balance the decreasing value of z. A temperature flux which acts against the temperature gradient is the thermal diffusivity, since it can be described with Fick's laws of diffusion. Furthermore, this is a variable which is not included into the list of governing parameters in section 2.6.2 due to the requirement $z \gg z_0$. In order to make a conclusion about the influence of thermal diffusivity on the temperature gradient, a quantitatively consideration is necessary. Besides, radiative and humidity effects can not be excluded (Gopalakrishnan et al., 1998).

6. Conclusions

Before the data of the thermocouples could be used for the calculation of the dimensionless gradients of temperature, their quality was assessed. It was found that there is a small systematic error for the temperature measurements outside transition periods which could be corrected considering the measurements form the portable station as valid. The time periods which were used for the assessment of M-O similarity theory were carefully chosen. Therefore horizontal homogeneity, steady state conditions and fair weather conditions were applied. To state fair weather conditions, account is made of the mesoscale wind system of the measurement area. In order to assume horizontal homogeneity, attention is paid to an undisturbed fetch, whereupon the small heterogeneity was not considered. Since no adequate method was found to state steady state conditions, the calculations of the dimensionless gradients were made for 15 minutes and 30 minutes averaging time periods. The comparison of the universal functions for the upper four thermocouples showed no significant difference between the two averaging time periods for stable stratification. For unstable stratification, the formulas differed.

By forcing the turbulent Prandtl number to a value of 0.95, it is possible to get rid of this difference, but the uncertainties in the fitting curves increase.
The comparison of the dimensionless gradients for stable stratification to the universal function from KANSAS experiment which was modified by Högström (1988) showed that there are large differences in the slope of the linear functions. The slope of the universal function from BLLAST campaign represents 22 % of the theoretical one.
The flux dependent variables were identified as parameters with the largest probability to be responsible for this difference. The calculation of constant 'correction factors' led to values of 2.16 for the turbulent heat flux and 2.15 for the friction velocity. Similar results could be derived analytically. Thus, in order to follow M-O similarity theory under stable conditions, it must be assumed that the eddy covariance station measures only half of the real turbulent fluxes at night. Furthermore, it was showed that the correction is unusable for the lowest measurement heights.
For thermocouples #1 to #3 no similarity was given which is consistent with literature. The measurement height #4 could be considered as a transition case, considering the ratio of the measurement height and the roughness length. A physical explanation of the deviations of the lowest thermocouples from the M-O similarity theory could be the influence of thermal diffusivity and radiative and humidity effects.

7. Outlook

It was not possible to assess the M-O similarity for unstable stratification because no adequate averaging time period could be found. For this reason, only the fluxes for stable stratification were corrected. It was shown that the predicted correction factors are not usable for both stratifications. Therefore effort should be put into the derivation of an adequate averaging time period for unstable stratifications for which 'correction factors' has to be derived, too. If these correction factors show large differences to the ones predicted for stable stratification, it should be checked if there could be a dependence of these factors on an other atmospheric parameter. In this case, it should be possible to develop a correction function which is valid for the whole stability range. In any case, the correction of the fluxes has to be verified. Its possible sources of error can occur in the data processing and in the measurement itself. So it is necessary to take a look into the data processing of the fluxes and to do an intensive literature research.
After a satisfying correction method is predicted for both stability ranges, it would be further interesting to investigate the dimensionless gradients for the lower measurement heights for stable and unstable stratification, respectively. In a first analysis it should be checked if a second order polynomial in z direction is the right strategy to interpolate the temperature profiles in this layer. If the results are consistent with the dimensionless gradients shown in this bachelor thesis, two main variables have to be assessed referring their influence on the flux-profile relationship for lower measurement heights. These two variables are molecular diffusivity and the roughness length z_0. Both were excluded as governing parameters in the derivation of the M-O similarity theory, because $z \gg z_0$

was required. But since this is not given for the lowest measurement heights, the neglect is not valid any more. If both were detected as governing parameters, this would led to seven governing parameters and three dimensions. So a modified M-O similarity theory has to be found which includes $m - n = 4$ independent parameters. In order to check if the molecular diffusivity comes into consideration as governing parameter, it would be helpful to calculate its value and compare it to the order of magnitude of the turbulent heat flux.

To develop a modified M-O similarity theory, a second measurement campaign with the same set up should be performed. The reasons for this is that at first the repeatability of the theory has to be checked and secondly it should be shown that the installation problems of the thermocouples are not responsible for the deviations and were successfully corrected in this bachelor thesis.

8. Acknowledgements

Die Messdaten, die in dieser Bachelorarbeit verwendet wurden, stammen von der Universität der Balearen und der Universität Bergen. Aus diesem Grund möchte ich mich ausdrücklich bei Prof. Joan Cuxart und Prof. Joachim Reuder dafür bedanken, dass sie mir ihre Daten bereit gestellt haben und ich die Erlaubnis hatte, diese in meiner Bachelorarbeit zu verwenden.

Ein herzlicher Dank geht an Prof. Jens Bange, für seine Unterstützung, vor allem gegen Ende der Bachelorarbeit. Er hat stets die Zeit gefunden, meine Fragen zu beantworten und mich mit gewinnbringenden Ideen versorgt.

Nicht weniger dankbar bin ich Dr. Daniel Martinez, der meine Bachelorarbeit betreut hat und mir dieses Thema vorgeschlagen hat. In unseren wöchentlichen Treffen hat er sich immer die Zeit genommen ausführlich auf meine Fragen zu antworten. Er hat viel Wert auch eine saubere Arbeitsweise gelegt, die ich ohne ihn nicht hätte einhalten können.

Ich möchte mich außerdem bei meiner Patentante, meinem großen Bruder und meiner ehemaligen Englischlehrerin dafür bedanken, dass sie mir mit dem Englisch geholfen haben.

Dankbarkeit gilt auch meinem kleinen Bruder, der mir seinen Laptop zur Verfügung gestellt hat. Ohne diesen wäre die Datenauswertung um einiges Zeitintensiver ausgefallen.

References

Barenblatt, G. and Monin, A. (1979). Similarity laws for turbulent stratified shear flows. *Archive for Rational Mechanics and Analysis*, 70(4):307–317.

Bernhardt, K.-H. (1995). Zur interpretation der monin-obuchovschen länge. *Meteorologische Zeitschrift*, 4(2):81–82.

Busch, N. E. (1973). The surface boundary layer. *Boundary-Layer Meteorology*, 4(1):213–240.

Businger, J. (1988). A note on the businger-dyer profiles. In *Topics in Micrometeorology. A Festschrift for Arch Dyer*, pages 145–151. Springer.

Businger, J., Wyngaard, J., Izumi, Y., and Bradley, E. (1971). Flux-profile relationships in the atmospheric surface layer. *Journal of the Atmospheric Sciences*, 28(2):181–189.

CR1000 (2011). *CR1000 Measurement and Control System.* Campbell Scientific, Inc. (CSI), 815 West 1800 North, Logan, Utah 84321, United States.

Dyer, A. (1974). A review of flux-profile relationships. *Boundary-Layer Meteorology*, 7(3):363–372.

Etling, D. (2008). *Theoretische Meteorologie : eine Einführung.* Springer, Berlin, 3., erw. und aktualisierte aufl. edition.

ExPlans (2011). *BLLAST Boundary-Layer Late Afternoon and Sunset Turbulence.* Experimental Plans.

Foken, T. (2006). *Angewandte Meteorologie : mikrometeorologische Methoden.* Springer, Berlin, 2., überarb. u. erw. aufl. edition.

Foken, T. and Skeib, G. (1983). Profile measurements in the atmospheric near-surface layer and the use of suitable universal functions for the determination of the turbulent energy exchange. *Boundary-Layer Meteorology*, 25(1):55–62.

Garratt, J. (1980). Surface influence upon vertical profiles in the atmospheric near-surface layer. *Quarterly Journal of the Royal Meteorological Society*, 106(450):803–819.

Garratt, J. (1983). Surface influence upon vertical profiles in the nocturnal boundary layer. *Boundary-Layer Meteorology*, 26(1):69–80.

Garratt, J. R. (1994). *The atmospheric boundary layer.* Cambridge university press.

Gavrilov, A. and Petrov, Y. S. (1981). Evaluation of the accuracy of determining turbulent fluxes from routine hydrometeorological measurement over sea. *Meteorology and Hydrology*, 4:52–59.

Gopalakrishnan, S., Sharan, M., McNider, R., and Singh, M. (1998). Study of radiative and turbulent processes in the stable boundary layer under weak wind conditions. *Journal of the atmospheric sciences*, 55(6):954–960.

Högström, U. (1982). A critical evaluation of the aerodynamical error of a turbulence instrument. *Journal of Applied Meteorology*, 21:1838–1844.

Högström, U. (1985). Von kármán's constant in atmospheric boundary layer flow: Reevaluated. *Journal of atmospheric sciences*, 42:263–270.

Högström, U. (1988). Non-dimensional wind and temperature profiles in the atmospheric surface layer: A re-evaluation. *Boundary-Layer Meteorology*, 42(1):55–78.

Högström, U. (1996). Review of some basic characteristics of the atmospheric surface layer. *Boundary-Layer Meteorology*, 78(3):215–246.

Jimenez, M. and Cuxart, J. (2012). The basin and local contributions of the flow over lannemezan seen by the mesonh model. Universitat de les Illes Baleares.

Kramm, G. and Herbert, F. (2009). Similarity hypotheses for the atmospheric surface layer expressed by non-dimensional characteristic invariants-a review. *The Open Atmospheric Science Journal*, 3:48–79.

Lee, X., Massman, W., and Law, B. E. (2004). *Handbook of micrometeorology: a guide for surface flux measurement and analysis*, volume 29. Springer.

Liljequist, G. H. and Cehak, K. (2007). *Allgemeine Meteorologie*. Springer.

Martinez, D. (2011). *Topograhically induced flows and nocturnal cooling in the atmospheric boundary layer*. PhD thesis, Universiat de les Illes Balears.

Martinez, D., Molinos, F., and Cuxart, J. (2012). Evolution of the temperature profile within the surface layer under stable conditions during the bllast campaign. Technical report, Physics Dept., Universitat Illes Balears, Palma, Mallorca, Spain.

McPherson, G. (1990). Statistics in scientific investigation: its basis, application, and interpretation.

Monin, A. and Obukhov, A. (1954). Basic laws of turbulent mixing in the surface layer of the atmosphere. *Trudy Geofiz. Inst. Acad. Nauk SSSR*, 24(151):163–187.

Nicholls, S. and Smith, F. (1982). On the definition of the flux of sensible heat. *Boundary-Layer Meteorology*, 24(1):121–127.

Oke, T. R. (1988). *Boundary layer climates*. Routledge.

Panofsky, H. A. (1963). Determination of stress from wind and temperature measurements. *Quarterly Journal of the Royal Meteorological Society*, 89(379):85–94.

Stull, R. B. (1988). *An introduction to boundary layer meteorology*, volume 13. Springer.

Tschalikov, D. (1968). O profilja vetra i temperatury v prizemnom sloe atmosfery pri ustojtschivoj stratifikacii. *Trudy Glavny Geofiziceskij observatorii*, 207:170–173.

Wyngaard, J. (1981). The effects of probe-induced flow distortion on atmospheric turbulence measurements. *Journal of Applied Meteorology*, 20(7):784–794.

Wyngaard, J. C. (2010). *Turbulence in the Atmosphere*. Cambridge University Press.

Yaglom, A. (1977). Comments on wind and temperature flux-profile relationships. *Boundary-Layer Meteorology*, 11(1):89–102.

Zilitinkevich, S. and Chalikov, D. (1968). Determining the universal wind-velocity and temperature profiles in the atmospheric boundary layer. *Izv. Atmospheric and Oceanic Physics*, 4(3):165–169.

Zilitinkevich, S. and Tschalikov, D. (1968). Opredelenie universalnych profilej skorosti vetra i temperatury v prizemnom sloe atmosfery (determination of universal profiles of wind velocity and temperature in the surface layer of the atmosphere). *Izv. AN SSSR, Fiz. Atm. i Okeana*, 4:294–302.

A. Appendix

A.1. Statistics

In the bachelor thesis, the root mean squared error $RMSD$, R^2 and R^2_{adj} are used to describe the fitted functions statistically. These statistic methods consist mainly of the total sum of squares TSS and the residual sum of squared ESS and their mean values.

$$TSS = \sum_{i=1}^{N} (y_i - \overline{y}_i)^2$$
$$ESS = \sum_{i=1}^{N} (y_i - \hat{y}_i)^2$$

where y_i is the measured variable, $\hat{y}_{x,i}$ its value in the model, $\overline{y}$ the mean value of all measured variables and N the number of variables. The total mean squares TMS and the residual mean squares EMS are defined as:

$$TMS = \frac{1}{N-p} TSS$$
$$EMS = \frac{1}{N} ESS$$

where p is the degree of the model. A linear function is a model of first order whereas the model used for the calculation of the temperature profiles in section 4.2 is of second order. The root mean squared error $RMSD$ is used as the uncertainty in percent for the fitted universal functions. It is defined as the extracted root of the residual mean square EMS:

$$RMSD = \sqrt{ESS}$$

Since there is no scaling of this error, it is only used here to compare the uncertainty of the fitted universal functions among each other.
The coefficient of multiple determination R^2 is defined as:

$$R^2 = \frac{TSS - ESS}{TSS}$$

It is used for the estimation of the goodness of the correction function for the temperature measured by the thermocouples. It takes values between zero and one, whereupon a value of one means perfect fit. R^2_{adj} is used in order to estimate the goodness of the fitted temperature gradients. It is calculated with

$$R^2_{adj} = (TMS - EMS)/TSS$$

In contrast to R^2 it can also take negative values, but the interpretation is similar. This means a value of one for R^2_{adj} means that the data fit perfectly to the given second-order polynomial (McPherson, 1990).

A.2. Several universal functions

	15 minutes average	$RMSD$ \%	30 minutes average	$RMSD$ \%
#1	$0.767 - 94.5\varsigma$	16.0	$0.75 - 87.95\varsigma$	15.3
	(0.712, 0.821) (-109, -79.8)		(0.678, 0.825) (-108, -68.2)	
#2	$0.787 - 8.66\varsigma$	12.3	$0.772 - 7.22\varsigma$	10.0
	(0.745, 0.829) (-12.5, -4.87)		(0.724, 0.82) (-11.5, -2.90)	
#3	$0.796 + 1.175\varsigma$	11.9	$0.7814 + 1.832\varsigma$	9.37
	(0.756, 0.837) (-1.02, 3.37)		(0.736, 0.826) (-0.587, 4.25)	
#4	$0.807 + 4.80\varsigma$	12.7	$0.793 + 5.02\varsigma$	10.7
	(0.764, 0.851) (3.55, 6.05)		(0.0536, 0.226) (-43.9, -31.2)	
#5	$0.821 + 4.62\varsigma$	15.3	$0.807 + 4.64\varsigma$	14.5
	(0.769, 0.873) (3.91, 5.32)		(0.738, 0.877) (3.71, 5.57)	
#6	$0.831 + 3.67\varsigma$	17.8	$0.817 + 3.653\varsigma$	17.8
	(0.771, 0.892) (3.19, 4.15)		(0.732, 0.903) (2.98, 4.32)	
#7	$0.8442 + 2.44\varsigma$	21.6	$0.817 + 2.43\varsigma$	17.8
	(0.771, 0.918) (2.16, 2.73)		(0.732, 0.903) (2.98, 4.32)	
#8	$0.855 + 1.63\varsigma$	25.2	$0.842 + 1.60\varsigma$	27.0
	(0.770, 0.941) (1.45, 1.81)		(0.712, 0.972) (1.33, 1.87)	

Table A.1: *Universal functions from BLLAST campaign for the stable case, $\kappa = 0.4$. Additionally the table contains the 95 % confidence intervals in brackets. $RMSD$ gives the uncertainty in percent. The functions given in this table has the form: $Pr_t + \gamma_2 \cdot Pr_t \cdot \varsigma$.*

	15 minutes average	$RMSD$ \%	30 minutes average	$RMSD$ \%
#1	$(0.0791 - 190\varsigma)^{-1/2}$	29.8	$(0.106 - 157\varsigma)^{-1/2}$	24.8
	(0.0133, 0.145) (-235, -145)		(-0.00323, 0.215) (-235, -78.6)	
#2	$(0.1003 - 83.6\varsigma)^{-1/2}$	22.6	$(0.126 - 71.6\varsigma)^{-1/2}$	18.2
	(0.0274, 0.178) (-101, -66.4)		(0.00804, 0.243) (-101, -42.4)	
#3	$(0.117 - 57.9\varsigma)^{-1/2}$	19.4	$(0.136 - 50.6\varsigma)^{-1/2}$	15.3
	(0.0374, 0.197) (-68.8, -47.0)		(0.0160, 0.256) (-68.9, -32.3)	
#4	$(0.140 - 37.6\varsigma)^{-1/2}$	15.3	$(0.149 - 33.8\varsigma)^{-1/2}$	11.9
	(0.0536, 0.226) (-43.9, -31.2)		(0.0281, 0.271) (-44.0, -23.5)	
#5	$(0.177 - 22.7\varsigma)^{-1/2}$	12.2	$(0.165 - 21.3\varsigma)^{-1/2}$	8.52
	(0.0796, 0.275) (-26.1, -19.4)		(0.0412, 0.289) (-26.4, -16.2)	
#6	$(0.214 - 16.3\varsigma)^{-1/2}$	10.7	$(0.174 - 15.8\varsigma)^{-1/2}$	7.31
	(0.0981, 0.329) (-18.7, -14.0)		(0.0332, 0.315) (-19.3, -12.26)	
#7	$(0.280 - 11.0\varsigma)^{-1/2}$	10.6	$(0.174 - 15.8\varsigma)^{-1/2}$	7.31
	(0.100, 0.459) (-12.8, -9.21)		(0.0332, 0.315) (-19.3, -12.26)	
#8	$(0.362 - 8.19\varsigma)^{-1/2}$	12.3	$(0.506 - 8.76\varsigma)^{-1/2}$	10.4
	(0.0360, 0.689) (-9.98, -6.41)		(-0.309, 0.609) (-12.2, -5.19)	

Table A.2: *Universal functions from BLLAST campaign for the unstable case, $\kappa = 0.4$. Additionally the table contains the 95 % confidence intervals in brackets. $RMSD$ gives the uncertainty in percent. The formulation of the universal functions in this table follow the form: $(1 \cdot Pr_t^{-2} - \gamma_1 \cdot Pr_t^{-2} \cdot \varsigma)^{-1/2}$.*

Averaging Period	Formulation	$RMSD$ %	stratification
15 min	$1.40(1 - 20.9\varsigma)^{-1/2}$	13.8	$\varsigma < 0$
	(1.42, 1.41) (-23.0, -18.7)		
30 min	$1.74(1 - 36.9\varsigma)^{-1/2}$	12.5	$\varsigma < 0$
	(2.14, 1.501) (-43.2, -29.4)		
15 min	$0.955 \cdot (1 + 1.79\varsigma)$	24.8	$\varsigma \geq 0$
	(0.920, 0.990) (1.65, 1.93)		
30 min	$0.947 \cdot (1 + 1.76\varsigma)$	25.3	$\varsigma \geq 0$
	(0.897, 0.996) (1.58, 1.95)		

Table A.3: *Universal functions for thermocouples #5 to #8 for both time periods. Additionally the 95 % confidence intervals are given in brackets. $RMSD$ is used as uncertainty in percent.*

Author	κ_{original}	Φ_H	$\Phi_{H\text{modified}}$	Comments
Tschalikov (1968)	0.4	$1 + 5.71\varsigma$	-	$\varsigma > 0.04$
Zilitinkevich and Chalikov (1968)	0.43	$1 + 9.9\varsigma$	$0.95 + 8.9\varsigma$	
Businger et al. (1971)	0.35	$0.74 + 4.7\varsigma$	$0.95 + 7.8\varsigma$	
Dyer (1974)	0.41	$1 + 5\varsigma$	$0.95 + 4.5\varsigma$	
Gavrilov and Petrov (1981)	0.4	$0.9 + 6\varsigma$	-	

Table A.4: *Various universal functions which appears in the literature for stable stratification. The formulation are modified by Högström (1988) and are calculated for $Pr_t = 0.95$. The table is taken from Foken (2006).*

Author	κ_{original}	Φ_H	$\Phi_{H\text{modified}}$	Comments
(Zilitinkevich and Chalikov, 1968)	0.43	$1 + 1.45\varsigma$	$0.95 + 1.31\varsigma$	$-0.15 < \varsigma 0$
		$0.41(-\varsigma)^{-1/3}$	$0.40(-\varsigma)^{-1/3}$	$-1.2 < \varsigma - 0.15$
(Businger et al., 1971)	0.35	$0.74(1 - 9\varsigma)^{-1/2}$	$0.95(1 - 11.6\varsigma)^{-1/2}$	
(Dyer, 1974)	0.41	$(1 - 16\varsigma)^{-1/2}$	$0.95(1 - 15.2\varsigma)^{-1/2}$	

Table A.5: *Various universal functions which appears in the literature for unstable stratification. The formulation are modified by Högström (1988) and are calculated for $Pr_t = 0.95$. The table is taken from (Foken, 2006).*